Vol. 01 No. 04 2023

RiESTech

JOURNAL RECENT IN ENGINEERING SCIENCE AND TECHNOLOGY

MBI

E- ISSN : 2985-8321
P -ISSN : 2985-704X

Recent in Engineering Science and Technology (RiESTech)
PT MENCERDASKAN BANGSA INDONESIA (MBI)
Available online at: http://www.mbi-journals.com/index.php/riestech

E- ISSN : 2985-8321
P -ISSN : 2985-704X

Recent in Engineering Science and Technology (RiESTech)

Volume 1 No 4 Oktober 2023

FOCUS AND SCOPE

RIESTECH

Recent in Engineering Science and Technology **(RiESTech):** I*SSN: 2985-704X (print), ISSN: 2985-8321 (online)* a peer-reviewed quarterly engineering journal, publishes theoretical and experimental high-quality papers to promote engineering and technology's theory and practice. In addition to peer-reviewed original research papers, the Editorial Board welcomes original research reports, state-of-the-art reviews, and communications in the broadly defined field of recent engineering science and technology. **RiESTech** covers topics contributing to a better understanding of engineering, material science, computer science, environmental science, and their applications. **RiESTech** is concerned with scientific research on mechanical and civil engineering, Electrical/Electronics and Computer Engineering, and Metallurgical and Materials Engineering with specific analytical techniques and/or computational methods.

The frequency of RiESTech publications is four times a year namely in January, April, July, and October. The scope of RiESTech includes a wide spectrum of subjects namely:

Mechanical and Civil Engineering (Automotive Technologies; Construction Materials; Design and Manufacturing; Dynamics and Control; Energy Generation, Utilization, Conversion, and Storage; Fluid Mechanics and Hydraulics; Heat and Mass Transfer; Micro-Nano Sciences; Renewable and Sustainable Energy Technologies; Robotics and Mechatronics; Solid Mechanics and Structure; Thermal Sciences)

Electrical/Electronics and Computer Engineering (Instrumentation; Coding, Cryptography, and Information Protection; Communications, Networks, Mobile Computing, and Distributed Systems; Compilers and Operating Systems; Parallel Processing, and Dependability; Computer Vision and Robotics; Control Theory; Electromagnetic Waves, Microwave Techniques and Antennas; Embedded Systems; Integrated Circuits, VLSI Design, Testing, and CAD; Microelectromechanical Systems; Microelectronics, and Electronic Devices and Circuits; Power, Energy and Energy Conversion Systems; Signal, Image, and Speech Processing; Machine Learning and Data Science)

E- ISSN : 2985-8321
P -ISSN : 2985-704X

Metallurgical and Materials Engineering (Advanced Materials Science; Ceramic and Inorganic Materials; Electronic-Magnetic Materials; Energy and Environment; Materials Characterization; Metallurgy Extractive; Polymers and Nanocomposites)

Environmental Science and Engineering (Waste Management, Climate Change, Zero Waste, Environmental Disaster Management, Circular Economy, Sustainable Development, Environmental Security, Environmental Management, Environmental Ecology, Conservation of Natural Resources And Environment, Environmental Impact Analysis, Planning and Environmental Administration, Environmental Health, Environmental Pollution, Environmental Accounting, and Environmental Information Systems)

Recent in Engineering Science and Technology (RiESTech)
PT MENCERDASKAN BANGSA INDONESIA (MBI)
Available online at: http://www.mbi-journals.com/index.php/riestech

E- ISSN : 2985-8321
P -ISSN : 2985-704X

Recent in Engineering Science and Technology

(RiESTech)

Volume 1 No 4 Oktober 2023

Recent in Engineering Science and Technology (RiESTech)
PT MENCERDASKAN BANGSA INDONESIA (MBI)
Available online at: http://www.mbi-journals.com/index.php/riestech

E- ISSN : 2985-8321
P -ISSN : 2985-704X

Layout and Typesetting:

Imam Sapto Nugroho, Universitas Indonesia (Alumni), Indonesia
Kamil Raihan Permana, Universitas Indonesia, Indonesia
Raihan Trinanda Agsya, Politeknik Negeri Jakarta, Indonesia

PUBLISHER
PT MENCERDASKAN BANGSA INDONESIA (MBI)
Address : 4th Floor Gedung STC Senayan Room 31-34, Jl. Asia Afrika Pintu IX, Jakarta 10270, Indonesia.

Recent in Engineering Science and Technology (RiESTech)
PT MENCERDASKAN BANGSA INDONESIA (MBI)
Available online at: http://www.mbi-journals.com/index.php/riestech

E- ISSN : 2985-8321
P -ISSN : 2985-704X

Recent in Engineering Science and Technology (RiESTech)

Volume 1 No 4 Oktober 2023

PREFACE

Journal RiESTech (p-ISSN: 2985-704X (print), e-ISSN: 2985-8321 (online); is a peer review journal published by PT Mencerdaskan Bangsa Indonesia. The RiESTech journal is published four times a year in January, April, July, and October. This journal provides direct open access to its content on the principle that making research freely available to the public supports a greater global exchange of knowledge within the engineering field. This journal aims to provide a place for academics, researchers, and practitioners to publish original research articles or review articles. The scope of articles published in this journal relates to various topics in the field of outcomes of research activities.

The RiESTech journal publishes papers strictly following the RiESTech guidelines and templates for manuscript preparation. All submitted manuscripts will go through a double-blind peer review process. The paper is read by members of the editor (according to the area of specialization) and will be screened by the Managing Editor to meet the criteria required for RiESTech publication. Manuscripts will be sent to two reviewers based on their historical experience in reviewing manuscripts or based on their areas of specialization. RiESTech has review forms to keep the same item reviewed by two reviewers. Then the editorial board makes a decision on the comments or suggestions of the reviewers.

Reviewers provide an assessment of originality, clarity of presentation, contribution to the field/science. This journal publishes research articles, review articles/literature reviews, case reports and concept/policy articles, in all fields of Computer Science, Informatics Engineering, Multimedia, Arts. The article to be published is an original work and has never been published. Incoming articles will be reviewed by the reviewer team.

The Editorial Board will try to continue to improve the quality of the journal so that it can become an important reference in the development of engineering sciences. The greatest appreciation and gratitude to Mitra Bestari along with members of the Editorial Board and all parties involved in the publication of this journal. Complete writing instructions are displayed on the portal of this journal.

Regards,

Chief Editor

Recent in Engineering Science and Technology (RiESTech)
PT MENCERDASKAN BANGSA INDONESIA (MBI)
Available online at: http://www.mbi-journals.com/index.php/riestech

E- ISSN : 2985-8321
P -ISSN : 2985-704X

Recent in Engineering Science and Technology (RiESTech)

Volume 1 No 4 Oktober 2023

Contents

Articles

RiESTech
Recent in Engineering Science and Technology

MBI

Article

The electrical properties of composite fabricated of carbon-phenol formaldehyde

Agus Edy Pramono [1*], Yohannes PatrickR [1], Belyamin [1], Nanik Indayaningsih [2]

[1] Magister Program in Applied Manufacturing Technology Engineering, Politeknik Negeri Jakarta, Jl. Prof. Dr. G.A. Siwabessy, Kampus UI, Depok 16425, Jawa Barat, Indonesia
[2] Research Centre for Physics, National Research, and Innovation Agency (BRIN), Kawasan Puspiptek, Gd. 440-442, Tangerang Selatan, Banten 15310, Indonesia
* Correspondence: agus.edypramono@mesin.pnj.ac.id

Abstract: This research aimed to create composites of carbon-phenol formaldehyde (PF) using carbonated rice husks as fillers. The composites showed electrical conductivity that increased with carbon content and decreased electrical resistance. The composites were evaluated for their physical, and electrical properties. The results showed that increasing PF content resulted in higher density but lower porosity, making the composites heavier. Specimens with 80% carbon weight and 20% PF weight produce an electrical conductivity of 0.055 [S/cm], while those with 70% carbon weight and 30% PF weight produce an electrical conductivity of 0.039 [S/cm]. Specimens with 60% carbon weight and 40% PF weight generate an electrical conductivity of 0.013 [S/cm].

Keywords: Rice husks carbon; Carbon-phenol formaldehyde (PF) composite; Polymer electrically conductive; electrical properties.

Citation:. Pramono, A. E., Patrick, Y. P., Belyamin, & Indayaningsih, N. I. (2023). The electrical properties of composite fabricated of carbon-phenol formaldehyde. Recent in Engineering Science and Technology, 1(04). Retrieved from https://www.mbi-journals.com/index.php/riestech/article/view/29

Academic Editor: Iwan Susanto

Received: 26 September 2023
Accepted: 23 Oktober 2023
Published: 26 Oktober 2023

Publisher's Note: MBI stays neutral with regard to jurisdictional claims in published maps and institutional affiliations.

1. Introduction

The study aimed to engineer the properties of composites made from rice husks carbon and phenol formaldehyde (PF) matrix. The study focused on developing electrically conductive parts using carbon - PF composites. Composite engineering research with polymer matrices and carbon fillers has been widely studied by researchers for decades.

This article explores the use of CFRP composites with a resin matrix modified by acrylonitrile nano rubber. The study demonstrates that incorporating nano rubber improves the fracture toughness and interlaminar shear strength of CFRP composites. SEM analysis indicates that these enhancements result from nano rubber debonding, crack path deflection, and fiber bridging [1]. This article explores the synthesis of PPy/CuZnFe2O4 nanocomposites and their impact on physical, mechanical, and electrical properties. Using in-situ polymerization with Ammonium Persulphate as the oxidizing agent, the research reveals that incorporating nanoparticles alters the structure and conductivity of the composite. This highlights their potential as excellent insulation materials for electrical and electronic applications [2]. This article explores carbon-quartz fiber-reinforced phenolic-silica aerogel nanocomposites (C-QF/PSi) for lightweight thermal protection. They offer strong compression resistance, low thermal conductivity, and excellent thermal ablation and insulation properties. These nanocomposites have promising applications in aerospace and other thermal protection fields [3]. This study develops PA66/CF composites with a hybrid filler of AGO and CNTs. The 2:1 ratio of AGO to CNTs improves interfacial shear strength, tensile strength, and storage modulus significantly compared to the control sample. The composite also exhibits high damping properties and strong CF-PA66 bonding due to hydrogen bonding, good dispersion, and the mechanical effects of the AGO-CNT hybrid [4]. This article explores electrically conductive polymer composites

with fillers like GR, CNTs, and CB in a PC/ABS matrix. CNTs show superior electrical and mechanical performance compared to other carbon-based fillers [5]. This research modifies high modulus carbon fibers (HMCF) using anodization and electrochemical grafting. The surface treatment with NH4HCO3 electrolyte enhances DETA grafting, while (NH4)2SO4 increases oxygen groups. These modifications greatly improve the interfacial performance of the HMCF/epoxy composite, boosting interlaminar shear strength by 257.1%. Valuable for high-performance applications utilizing modified HMCF [6]. This study introduces a homogenization model to analyze the processing of carbon-DCPD composites via frontal polymerization. The model identifies two distinct processing regimes based on the fiber volume fraction. Experimental validation of the model's predictions is performed on carbon-DCPD composite panels [7]. This study analyzes the failure of CFRP composites under fiber-aligned compression. Compressive strength is influenced by fiber and matrix properties, with shear stress playing a crucial role. Improving properties or reducing fiber misalignment enhances compressive strength by up to 3.38%. Matrix elasticity has the greatest influence, followed by fiber alignment and matrix plasticity [8]. This study compares carbon/carbon (C/C) composites with different carbon matrix development methods. Composites with PyCN matrix show the highest strength and toughness, while those with asphalt-derived carbon matrix have lower strength. PyCX matrix exhibits the highest thermal conductivity [9]. This research develops High Temperature Low-Sag (HTLS) conductors for high-temperature power transmission. Tests on carbon and glass fiber composite rods reveal that excessive compressive stress in the carbon region causes failure. Natural fiber deviation also impacts bending strength and damage initiation [10]. This research examines the mechanical properties of the matrix in carbon fiber-reinforced plastic composites (CFRP) to study stress concentration at the fiber-matrix interface caused by adjacent fiber fractures. The results reveal a linear correlation between crack tip opening displacement (CTOD) and stress concentration factor (SCF), informing the development of stronger CFRP materials [11]. This research investigates thermoplastic composites and their welding process with short durations. An experimental setup is devised to assess the adhesion of carbon-PEKK composites within time intervals ranging from 1 second to 1 hour. The findings identify three distinct bonding stages and shed light on the healing kinetics at the interface [12]. This research proposes an eco-friendly method to enhance the adhesion of carbon fiber-polymer composites using carboxymethyl cellulose (CMC) and graphene oxide (GO). The CMC and GO significantly improve the interfacial and interlayer shear strength of the composite, offering potential for enhancing its performance with natural cellulose fibers [13]. This study analyzes failures related to water in the polymer matrix and interfaces of composites and nanocomposites used in marine construction. By using experimental and simulation methods, the study investigates damages in polymer-based carbon nanotube (CNT) composites. The findings reveal the mechanisms of damage and highlight improvements in the water resistance properties of nanocomposites [14]. In this study, we examined thermoplastic overmolding methods on thermoset composites using epoxy resin and PA6. Factors investigated included fiber type, molding temperature, and peel-ply usage. Peel-ply, higher temperature, and carbon fiber reinforcement improved adhesion. Mechanical analysis and imaging techniques supported the findings [15]. This research explores the impact of temperature and relative humidity on the electrical resistance of carbon fibers in polymer composites. The findings emphasize the importance of considering these effects in carbon fiber resistance measurements for health monitoring purposes. It highlights the suitability of carbon fibers for diverse applications [16]. This research investigates the impact of surface treatment and sizing type on carbon fibers in polymer composites. PA6 pellets reinforced with short fibers were produced and analyzed. The results show that surface treatment and sizing type affect the modulus and flexural strength of

the composite [17]. This research compares the mechanical performance of recycled sheet materials using different methods. Sandwich panels show potential for upcycling, achieving properties similar to monolithic laminates. The recycling method also produces flat sheets without wrinkles, comparable to new materials [18]. This study developed a ceramifiable electroconductive polymer composite using glass powder, mica powder, organically modified montmorillonite, and short carbon fibers in EVA. The composite shows excellent EMI shielding and high-temperature resistance [19].

This new research project focuses on the engineering of carbon-phenol formaldehyde composites for electrical conductivity properties. The density, porosity, and morphology of the composite are also investigated.

2. Materials and Experiment Methods

2. 1 Sample Preparation

We produced this composite by combining carbon from rice husks and a phenol-formaldehyde (PF) matrix. The rice husks were carbonized at 950°C with a heating rate of 2°C/minute. Carbon was milled to a 150-mesh size, while PF powder was sieved through a 350-mesh sieve. Varying weight ratios (60:40, 70:30, and 80:20) of carbon and PF were mixed and heat-compacted at 120°C and 200 bars pressure for 15 minutes using a hydraulic press.

Other previous research has shown that the carbonization process results in highly conductive carbon (99.9%) [9]. Researchers and authors of this article have done carbonization of organic waste with the same technique before, but for different research [20].

2. 2 Material characteristics

The carbon structure is an amorphous structure with an irregular arrangement of atoms, and the peak intensity observed at $2\theta = 24.25°$. The carbon density was found to be 1.3794 ± 0.12 grams/cm^3. Another study showed a carbon fiber density of 1.76 g/cm^3. PAN-based carbon fiber without size agents (average diameter seven μm, density1. 78 g/cm^3) supplied by Heng Shen Industries, Inc. (Jiangsu, China) [13]. Sigrafil CT24-5.0/270-E100 carbon fibres 1.79 [g/cm^3] [16].

2. 3 Composite density-porosity tests

The density of carbon composites is determined follow the Archimedes method, based on the DIN-51097 standard to conduct the experiment [21, 22]. Porosity is defined as the percentage of the open pore volume in a specimen relative to its total exterior volume.

2. 4 Testing of electrical properties

The ASTM D4496 standard was followed to test the electrical conductivity using the four-point probe method. The Keithley Instruments' 2450 Source Meter® Instrument was used for the testing, which was conducted at the Research Centre for Physics, National Research, and Innovation Agency (BRIN), Indonesia. Similar methods have been used in other studies. Samples with electrical conductivity higher than 10^{-8} [S/cm] were tested using a 2400-meter source (Keithley, USA) and the standard four-probe method was used to record the results [19].

3. Results and Discussion

3.1. Composite density

The density of the composite material studied can be seen in Figure 1. The incorporation of more carbon in the composite led to a decrease in density, making the composite material lighter. This finding provides evidence that carbon is lighter than phenol-formaldehyde after undergoing hot compaction at 120 °C, compaction of 200 bars, and holding time of 15 minutes. Specifically, the carbon-PF composite sample with code C8-2PF (80% by weight of carbon and 20% by weight of phenol-formaldehyde) exhibited a density of 1.11 [grams/cm^3]. On the other hand, increasing the PF content resulted in a higher composite density, as demonstrated by the sample code C6-4PF (60% carbon weight and 40% PF weight) with a density of 1.42 [grams/cm^3]. The study conducted a comparison with other materials, revealing that the density of pp-GF virgin monolithic was 1.65 [grams/cm^3] and PA6-CF SMC coarse was 1.41 [grams/cm^3] [18]. C-QF/PSi results in density in the range of 0. 460 to 0. 515 [g/cm^3] [3].

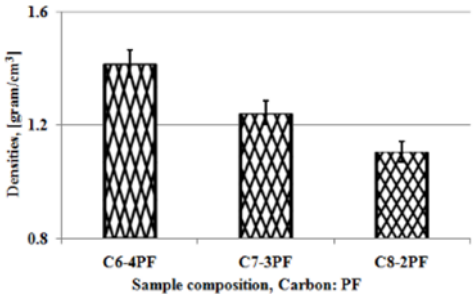

Figure 1. Densities of carbon-PF composite

3.2. Composite porosity

The heat compaction process of 120°C and 200 bar pressure is not sufficient to eliminate porosity in the carbon-PF composite bulk, as shown in Figure 2. Specifically, the samples with the code C8-2PF (80% by weight of carbon and 20% by weight of phenol-formaldehyde), which contained 80% carbon by weight, exhibited porosity levels of up to 0.8%. However, increasing the PF content in the composites can lead to a reduction in porosity. This is demonstrated by composites with sample code C6-4PF(60% carbon weight and 40% PF weight), which had a PF weight content of 40% and a porosity level of only 0.16%. It is important to note that the porosity of the CFRP samples in the other study was found to be less than 3% [8].

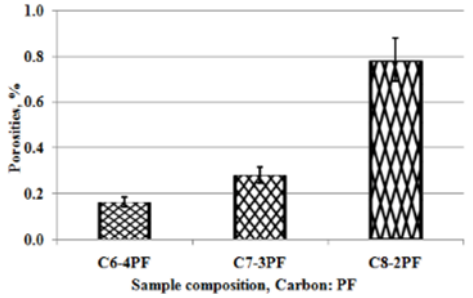

Figure 2. Porosities of carbon-PF composite

3.3. Density and porosity relationships

The relationship between density and porosity is evident, with a decrease in porosity corresponding to an increase in composite density, as shown in Figure 3. The C6-4PF composite exhibits low porosity (0.16%) and high density (1.42 g/cm^3). In contrast, the C8-2PF composite has a density of 1.11 g/cm^3 and a porosity of 0.8%. This suggests that increasing the carbon weight content leads to higher porosity in the composite. The performance of composite materials in rheology is influenced by factors such as interfacial adhesion between fillers and polymers, as well as the properties of densities and porosities. Additionally, particle size, distribution, shape, dispersion, and associated volume fractions can also have an impact [23].

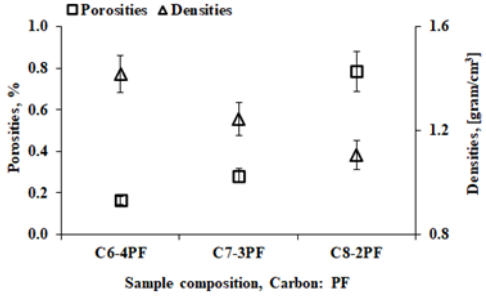

Figure 3. Densities and porossities relationship

The higher porosity observed in C8-2PF suggests that both the carbon content and rheological properties play a role in the formation of porosity. The 20% PF content, which cannot be uniformly dispersed within the composite bulk, leads to increased porosity. This likely explains the observed porosity in the composite material. There is a clear relationship between porosity and density. Porosity represents the percentage of void space in a material, while density refers to the mass per unit volume of the material. Generally, higher porosity results in lower density because porosity reduces the overall mass of the material without significantly affecting its volume. In other words, a more porous material will have a lower mass per unit volume, resulting in lower density. Sample C8-2PF exhibits the highest porosity (0.78%) and the lowest density (1.11 g/cm^3). On the other hand, sample C6-4PF demonstrates the lowest porosity (0.16%) and the highest density (1.42 g/cm^3). This inverse relationship between porosity and density is expected and can be used to predict the density of a material based on its porosity, or vice versa. The composite samples with higher weight percentages of carbon (C6-4PF) exhibit lower porosity and higher density compared to samples with lower weight percentages of carbon (C7-3PF and C8-2PF). This indicates that increasing the amount of carbon in the composite leads to a more compact and dense material with fewer voids or pores. While the difference in densities between the samples is relatively small, the difference in porosity is more significant. This suggests that the amount of carbon in the composite has a greater effect on porosity than on density. Factors affecting the porosity and density of composite materials can vary, as observed in this study. Porosity was influenced by the weight ratio of carbon and phenol-formaldehyde, while density remained relatively constant since the amount of resin used in the composite matrix was constant. The weight ratios of the composite materials (60:40, 70:30, and 80:20) significantly influenced the porosity of the resulting samples, as indicated by

the significant difference in means. This may be attributed to differences in the packing density of the carbon and PF particles at different weight ratios, affecting the formation of voids during heat compaction.

On the other hand, the weight ratios of the composite materials did not have a significant effect on the overall density of the resulting samples, as indicated by the lack of significant difference in means. This could be due to the constant PF matrix, which is the main contributor to density, while the weight ratio of the carbon particles varied.

3.4. Current and voltage of carbon-PF composite

The purpose of this study was to measure the electrical properties of a carbon-PF composite, specifically its ability to deliver electrical current and voltage. The measurements were conducted at the Research Centre for Physics, National Research, and Innovation Agency (BRIN), Indonesia, using the four-point probe method. A voltage speed of 0.16 V/second was set, ranging from -4 Volts to +4 Volts, to generate an electric current in Ampere, as shown in Figure 4.

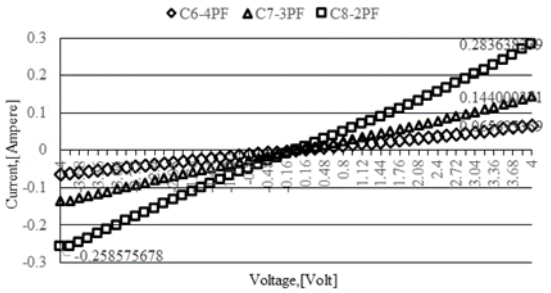

Figure 4. Electric current vs. voltage

For instance, in the case of specimen C8-2PF, a voltage value of 4 V allowed an electric current flow of 0.284 Ampere on the composite. The amount of electrical current decreased with a decrease in the carbon content of the composite. For example, specimen C7-3PF produced a current flow of 0.144 A at a voltage of 4 V, while specimen C6-4PF conducted an electric current of 0.065 A at the same voltage.

3. 5. Relationship between conductivity and electrical resistance

Simultaneously with the measurement of electric current by voltage setting, the electrical resistance value is also measured using the four-point probe method. Figure 5 shows that the electrical resistance value of a carbon-PF composite decreases with an increase in the volume of carbon content.

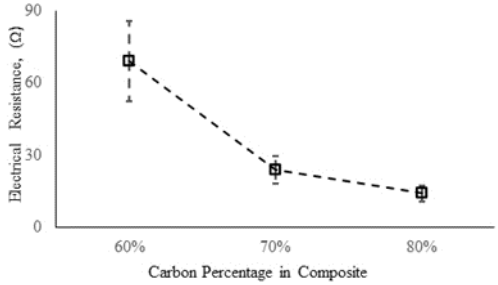

Figure 5. Electrical resistance vs. carbon content

For instance, specimens with a weight volume of 80% carbon exhibit an electrical resistance value of 14 Ω, while specimens with a weight volume of 70% carbon display a resistance value of 24 Ω. On the other hand, specimens with a weight volume of 60% carbon demonstrate a resistance of 69 Ω. These findings demonstrate that higher carbon content in the composite leads to a lower electrical resistance value, indicating that the carbon content can conduct electricity. This study of engineered materials provides evidence that increasing the carbon content results in a lower electrical resistance. The findings reveal that the volume resistivity decreases with an increase in the content of carbon-based fillers. This suggests that the addition of carbon-based fillers enhances the electrical conductivity of the PC/ABS composite material [5]. Figure 6 shows that the electrical conductivity of carbon-PF composites increases as the electrical resistance decreases. For instance, specimens coded as C8-2PF with 80% carbon weight volume and 20% PF weight produce an electrical conductivity of 0.055 [S/cm], while those coded as C7-3PF with 70% carbon weight volume and 30% PF weight produce an electrical conductivity of 0.039 [S/cm].

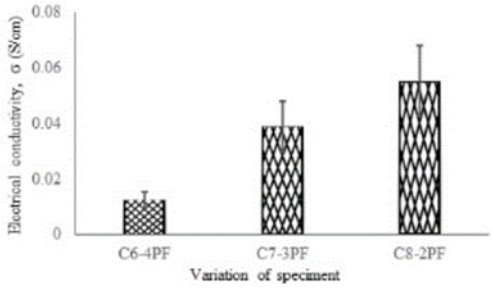

Figure 6. Electrical conductivity

Similarly, specimens with 60% carbon weight volume and 40% PF weight generate an electrical conductivity of 0.013 [S/cm], as seen in Figure 7. Thus, increasing the carbon weight volume leads to higher electrical conductivity in the carbon-PF composites of this study. In contrast, other studies have reported different electrical conductivity values for composite materials. For instance, the conductivity of Ethylene-vinyl acetate, Carbon fiber, organo-modified montmorillonite (EVA/CF/OMMT) composite is 4.44×10^{-15} S/cm, which is considered a typical insulating material. However, when short carbon fiber (SCF) is added to the EVA/CF/OMMT composite, the conductivity increases significantly. In the case of EVA/CF/OMMT/SCF 5(5%) composite, the conductivity rises to 4.74×10^{-9} S/cm [19]. Decreased electrical resistance leads to an increase in electrical conductivity. For instance, specimens with 60% carbon weight volume have a resistance of 69 Ω and an electrical conductivity of 0.013 [S/cm].

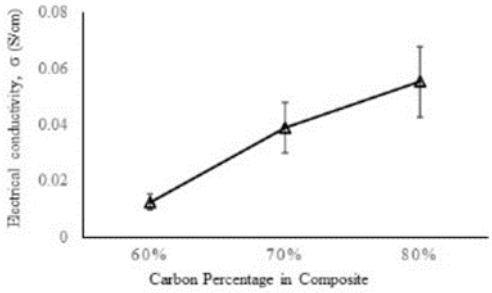

Figure 7. Electrical conductivity vs carbon content

Meanwhile, specimens with 70% carbon weight volume have a resistance of 24 Ω and an electrical conductivity of 0.039 [S/cm]. Specimens with 80% carbon weight volume have an electrical conductivity of 0.055 [S/cm] and a resistance of 14 Ω. Figure 8 demonstrates that there is a positive correlation between the volume of carbon weight and electrical conductivity, as well as a negative correlation between carbon volume and electrical resistance in the studied carbon-PF composite.

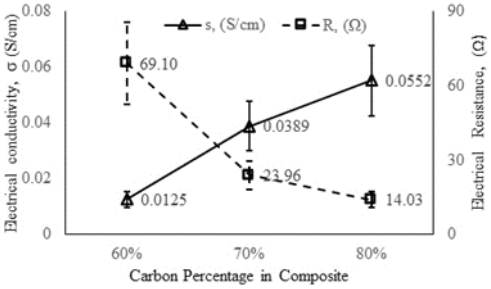

Figure 8. Carbon content vs. electrical conductivity vs. electrical resistance

When two substrates come in contact, surface roughness can prevent immediate perfect contact. The concept of intimate contact takes into account the initial surface roughness and the subsequent evolution of physical contact between the substrates [12]. This study found that the surface characteristics of carbon particles played a role in the rheological behavior of PF, resulting in the filling of porous cavities within the composite bulk, leading to an increase in the electrical resistance to flow.

4. Conclusions

Increasing the phenol-formaldehyde (PF) content in carbon-PF composites increases density. Sample C8-2PF has a density of 1.11 g/cm^3, while sample C6-4PF has a density of 1.42 g/cm^3. Higher carbon content results in lower density, making the composite lighter. Lower carbon content leads to weaker electrical conductivity. For example, specimen C8-2PF conducts 0.284 A of current at 4 V, while specimen C7-3PF conducts 0.144 A and specimen C6-4PF conducts 0.065 A at the same voltage. Sample C8-2PF (80% carbon, 20% PF) has an electrical conductivity of 0.055 S/cm, C7-3PF (70% carbon, 30% PF) has a conductivity of 0.039 S/cm, and samples with 60% carbon and 40% PF exhibit a conductivity of 0.013 S/cm.

Acknowledgment

Scheme of Leading Research of Product Innovation of DIPA of Politeknik Negeri Jakarta has funded this research, Contract Number: B.265/PL3.B/PN.00.03/2021, dated July 7, 2021. The author would like to thank UP2M, Politeknik Negeri Jakarta.

The authors acknowledge the facilities, scientific and technical support from Advanced Characterization Laboratories Serpong, National Research and Innovation Agency through E-Layanan Sains, Badan Riset dan Inovasi Nasional (BRIN).

References

1. Ozdemir, N. G. *et al.* Toughening of carbon fibre reinforced polymer composites with rubber nanoparticles for advanced industrial applications. *Express Polym. Lett.* **10**, 394–407 (2016).
2. Shanthala, V. S., Shobha Devi, S. N. & Murugendrappa, M. V. Synthesis, characterization and DC conductivity studies of polypyrrole/copper zinc iron oxide nanocomposites. *J. Asian Ceram. Soc.* **5**, 227–234 (2017).
3. Cheng, H., Fan, Z., Hong, C. & Zhang, X. Lightweight multiscale hybrid carbon-quartz fiber fabric reinforced phenolic-silica aerogel nanocomposite for high temperature thermal protection. *Compos. Part A Appl. Sci. Manuf.* **143**, 106313 (2021).
4. Cho, B. G. *et al.* Enhancement in mechanical properties of polyamide 66-carbon fiber composites containing graphene oxide-carbon nanotube hybrid nanofillers synthesized through in situ interfacial polymerization. *Compos. Part A Appl. Sci. Manuf.* **135**, 105938 (2020).
5. dal Lago, E. *et al.* Influence of different carbon-based fillers on electrical and mechanical properties of a PC/ABS blend. *Polymers (Basel).* **12**, (2020).
6. Fu, Y., Li, H. & Cao, W. Enhancing the interfacial properties of high-modulus carbon fiber reinforced polymer matrix composites via electrochemical surface oxidation and grafting. *Compos. Part A Appl. Sci. Manuf.* **130**, 105719 (2020).
7. Goli, E. *et al.* Frontal polymerization of unidirectional carbon-fiber-reinforced composites. *Compos. Part A Appl. Sci. Manuf.* **130**, 105689 (2020).
8. Li, A. J. *et al.* Effects of fiber and matrix properties on the compressive strength of carbon fiber reinforced polymer composites. *Xinxing Tan Cailiao/New Carbon Mater.* **35**, 752–761 (2020).
9. Liu, X. *et al.* Mechanical and thermal conduction properties of carbon/carbon composites with different carbon matrix microstructures. *Xinxing Tan Cailiao/New Carbon Mater.* **35**, 576–584 (2020).
10. Waters, D. H., Hoffman, J. D. & Kumosa, M. Effect of fiber misalignment on bending strength of pultruded hybrid polymer matrix composite rods subjected to bending and tension. *Compos. Part A Appl. Sci. Manuf.* **143**, 106287 (2021).

11. Yamamoto, G., Koizumi, K., Nakamura, T., Hirano, N. & Okabe, T. Tensile-strength-controlling factors in unidirectional carbon fiber reinforced plastic composites. *Compos. Part A Appl. Sci. Manuf.* **140**, 106140 (2021).

12. Avenet, J., Levy, A., Bailleul, J. L., Le Corre, S. & Delmas, J. Adhesion of high performance thermoplastic composites: Development of a bench and procedure for kinetics identification. *Compos. Part A Appl. Sci. Manuf.* **138**, (2020).

13. Qiu, B. *et al.* High micromechanical interlocking graphene oxide/carboxymethyl cellulose composite architectures for enhancing the interface adhesion between carbon fiber and epoxy. *Compos. Part A Appl. Sci. Manuf.* **139**, 106092 (2020).

14. Hu, Y., Ji, W. M. & Zhang, L. W. Water-induced damage revolution of the carbon nanotube reinforced poly (methyl methacrylate) composites. *Compos. Part A Appl. Sci. Manuf.* **136**, 105954 (2020).

15. Karakaya, N., Papila, M. & Özkoç, G. Overmolded hybrid composites of polyamide-6 on continuous carbon and glass fiber/epoxy composites: 'An assessment of the interface'. *Compos. Part A Appl. Sci. Manuf.* **131**, 105771 (2020).

16. Forintos, N. & Czigany, T. Reinforcing carbon fibers as sensors: The effect of temperature and humidity. *Compos. Part A Appl. Sci. Manuf.* **131**, (2020).

17. Hendlmeier, A., Simon, Ž., Chutani, A. & Henderson, L. C. Generating short carbon fiber polyamide-6 composites from continuous carbon fiber – A preliminary examination of surface treatment and sizing effects. *Compos. Part A Appl. Sci. Manuf.* **138**, (2020).

18. Kiss, P. *et al.* In-house recycling of carbon- and glass fibre-reinforced thermoplastic composite laminate waste into high-performance sheet materials. *Compos. Part A Appl. Sci. Manuf.* **139**, 106110 (2020).

19. Li, Y. M. *et al.* Carbon fiber-based polymer composite via ceramization toward excellent electromagnetic interference shielding performance and high temperature resistance. *Compos. Part A Appl. Sci. Manuf.* **131**, 105769 (2020).

20. Pramono, A. E. *et al.* Properties of ceramic fabricated of synthetic carbon and organoclay based on carbon particle size. *J. Ceram. Process. Res.* **21**, 465–478 (2020).

21. Katsuki, H. *et al.* Role of addition of kaolin on the firing of white clay for Korean porcelain. *J. Asian Ceram. Soc.* **8**, 492–501 (2020).

22. Riyap, H. I. *et al.* Microstructure and mechanical, physical and structural properties of sustainable lightweight metakaolin-based geopolymer cements and mortars employing rice husk. *J. Asian Ceram. Soc.* **7**, 199–212 (2019).

23. Watt, E., Abdelwahab, M. A., Mohanty, A. K. & Misra, M. Biocomposites from biobased polyamide 4,10 and waste corn cob based biocarbon. *Compos. Part A Appl. Sci. Manuf.* **145**, 106340 (2021).

RiESTech
Recent in Engineering Science and Technology

MBI

Article

Engineering and Process of Investment Casting for Pump Impellers

Arif Dermawan[1], Agus Edy Pramono[2*]

[1] Program studi perancangan, Jurusan Teknik Mesin, Politeknik Negeri Jakarta, Jl. Prof. G. A. Siwabessy, Kampus UI, Depok 16425, Indonesia
[2] Program studi Magister Terapan Rekayasa Teknologi Manufakturm Politeknik Negeri Jakarta, Jl. Prof. G. A. Siwabessy, Kampus UI, Depok 16425, Indonesia
* Correspondence: agus.edypramono@mesin.pnj.ac.id

Abstract: This article explains the investment casting process for manufacturing pump impellers. Investment casting is a metal casting process that utilizes ceramic molds. This system is employed to produce precise components compared to sand casting processes.

The fabrication of the metal pattern involves machining with dimensional adjustments. The dimensions are determined by adding the dimensional sizes, accounting for SS316L material shrinkage (2.5~3.5%), wax shrinkage (1%), and machining (5mm). The subsequent steps include wax injection to create wax patterns, the creation of a gating system, and ceramic sintering for molding. Wax patterns are produced separately for each part of the impeller and then assembled into a complete wax pattern that matches the impeller's geometry, including the gating system.

The wax patterns undergo multiple dipping cycles into slurry and stucco solutions, forming a thick ceramic layer around the wax impeller patterns. After the wax is melted from the ceramic mold, cavities are formed according to the impeller's geometry. Sintering the ceramic mold impeller at 1000°C results in a hard ceramic mold with cavities prepared to receive the molten metal.

The investment casting process for the pump impeller is now complete, and the pump impeller is further processed with precision machining to meet the specified dimensions, features, and geometry.

Keywords: Investment casting shell; pattern wax; ceramic shell; de-waxing; ceramic mold sintering

Citation:. Dermawan, A. & Edy Pramono, A. (2023). Engineering and Process of Investment Casting for Pump Impellers. Recent in Engineering Science and Technology, 1(04). Retrieved from https://www.mbi-journals.com/index.php/riestech/article/view/36

Academic Editor: Iwan Susanto

Received: 26 September 2023
Accepted: 16 Oktober 2023
Published: 29 Oktober 2023

Publisher's Note: MBI stays neutral with regard to jurisdictional claims in published maps and institutional affiliations.

1. Introduction

The purpose of this article is to elucidate the fabrication process and design of pump impellers through the utilization of the investment casting method.

Investment casting, a technique and process, offers an alternative to sand casting. Sand casting is a proficient method for rapid production, boasting low tooling costs and high design flexibility. However, it is imperative to take into consideration factors such as dimensional accuracy, surface quality, and specific defects within this process.

Investment casting serves as a method used to manufacture highly intricate and complex components or parts that are not feasible through other means. Investment casting has the capacity to produce components with precise dimensions, ideal for the manufacturing of extremely thin-sectioned parts. These parts exhibit a smooth final surface, negating the necessity for further finishing.

The investment casting technique has made significant contributions to transforming and modernizing the culture of ancient civilizations.

Investment casting played a pivotal role in technological evolution during World War II in the United States, as traditional machining processes couldn't meet the growing demand for wartime equipment. Investment casting was utilized to produce turbine blades and aircraft engines. The investment casting process has evolved from being a niche sector specializing in casting activities into a distinct industry [1].

This article aims to outline the steps involved in investment casting for the manufacturing of a pump impeller. It will also make reference to various articles that elucidate this process for comparative purposes.

In this study, Al2O3 powder with varying particle sizes was utilized as the matrix material. The creation of Ceramic-Inorganic Hybrid Composites (CIHCs) with different diameters involved the processes of stereolithography and gelcasting. Catalyst and initiator were introduced in the form of ammonium persulfate and N,N,N′,N′-tetramethyl ethylenediamine, respectively. The monomer, crosslinker, and dispersant employed included acrylamide, N,N′-methylenebisacrylamide, and sodium polyacrylate. Vacuum impregnation was carried out using a SiO2 solution, and deionized water was used to prepare the solutions in the experiments. Sodium alginate served as the thickening agent, while calcium phosphate, sodium hexametaphosphate, tribasic ammonium citrate, and hexane dioic acid were utilized for thickening Na-alginate [2].

In this study, Stereolithography (SL) and gel casting processes were utilized to create integral ceramic molds. SL prototypes were manufactured using photosensitive resin, and an alumina ceramic solution was prepared for the gel casting process. The ceramic solution was poured into the SL prototype and then polymerized to produce a green body. After the freezing, pre-curing, and post-treatment stages, the integral ceramic mold was successfully generated [3].

A ceramic mold, shaped like a shell, was prepared using filler materials, binders, anti-foaming agents, and moisturizing agents. These components included cobalt aluminate CA68 (C) as well as Zircon (-200#) (Z) and mullite (-200#) (M) as fillers. Two colloidal silica binders (SP 30 and SP ultra, referred to as binder A and binder B) were employed as binding agents. For mold creation, eight different types of ceramic solutions (MA, MA-C, MB, MB-C, ZA, ZA-C, ZB, and ZB-C) were formulated with the same composition. Solutions containing mullite filler and colloidal silica binders A and B were labeled as MA and MB, while those containing cobalt aluminate were denoted as MA-C and MB-C [4].

In this research, two shell molds (one from shell system I and one from shell system II) were utilized to produce LPT blades. The casting process was executed using a specialized solution under identical conditions. After the shell formation process, drying, wax removal, and heating procedures were carried out to enhance the strength of the shells. The melting and casting processes took place in a vacuum induction melting furnace, employing a nickel-based superalloy. The entire process was conducted within a controlled environment with a vacuum atmosphere. The end results comprised the shell molds and LPT blade components from both shell systems I and II [5].

This research involved the production of AlSi7Mg test blades through a combination of low-pressure die casting and ultrasonic refinement. This integrated technique yielded cast samples that were free from gas porosity and solidification defects, while also improving the mechanical properties of the alloy. The study indicates that the porosity observed is primarily a result of shrinkage, as evidenced by its irregular shape and its location among dendrites. The size of this porosity varies considerably. Round gas porosities were not detected, affirming the high effectiveness of ultrasonic degassing. Notably, the ultrasonic treatment significantly enhanced the mechanical properties of the alloy, particularly in terms of ductility. It is clear that the ultimate tensile strength, yield strength, and elongation experienced significant increases due to ultrasonic processing [6].

The existing stent manufacturing process is costly and encounters thermal challenges during laser cutting. There is a need to develop a new alternative for stent production,

especially when using magnesium alloys. In this study, a hybrid approach involving additional manufacturing techniques and investment casting within ceramic molds is utilized to efficiently and economically produce stents made of magnesium alloys [7].

In this study, the injection molding method is utilized to produce high-precision cores. This process comprises four stages: raw material preparation, element formation, adhesive removal, and sintering. The powder composition and particle size distribution are optimized to ensure the desired density after sintering. The primary raw material is liquid silica glass or quartz glass, known for its excellent thermal properties. Boron glass is introduced to enhance core sintering. Additional materials like ZrSiO4 and Al2O3 are employed to reduce sintering shrinkage and enhance the core's dimensional stability during casting with liquid metal. Sintering is carried out at a maximum temperature of 1250 °C, with a temperature rise rate of 50 °C/hour and cooling at 100 °C/hour [8].

Deformation in hollow turbine castings is influenced by various interrelated factors. Turbine geometry can be determined through measurements or by using solidification simulation software. Geometric data can be represented in STL format for rapid prototyping and computer-aided manufacturing [9].

This research explores thermal resistance at the casting-mold interface to advance technology and reduce defects in investment casting. In this study, an analysis of thermal resistance at the casting-mold interface was conducted using the inverse heat conduction method. It was found that the heat transfer coefficient at the casting-mold interface is highest when the alloy is in the liquid state and then decreases significantly during solidification. A proposed mechanism for the formation of gaps between the ceramic mold and the casting is based on the formation of mixed oxide layers at the interface. Based on numerical simulations, it was determined that this heat transfer coefficient has a smaller impact on the cooling rate of the casting compared to mold thickness, thermal conductivity, and emissivity [10].

In this research, recycled foundry sand (WFS) is used to prepare insulating refractory materials. Additional ingredients such as kyanite, alumina, and plastic clay are incorporated to improve the refractory properties. The inclusion of wood powder is intended to create pores and enhance the material's porosity [11].

Porous ceramics have gained attention due to their lightweight properties, low thermal conductivity, high porosity, large surface area, and resistance to thermal shock. In this study, cornstarch is introduced into a suspension containing Al2O3, SiO2, and MgO powders to create a homogeneous ceramic powder mixture. The primary material used is α-Al2O3 powder, with silica and MgO powders serving as sintering aids. Cornstarch functions as both a pore-forming agent and a binder, while an adhesive is created using a polyvinyl alcohol solution [12].

Reference studies indicate that most casting processes are conducted for aluminum materials. In this study, the closed pump impeller processed through investment casting is made of SS316L.

This article provides an in-depth exploration of the engineering and investment casting process for pump impellers, with a primary emphasis on the investment casting procedure. The manufacturing of the closed impeller is accomplished through investment casting, adhering to the API 610 standards.

2. Materials and Experiment Methods

The investment casting process is often used to create complex metal products, details and smooth surfaces. Such as engine parts, turbines, impellers and so on.

The general steps in the investment casting process are explained as follows:

1. Making dies from machining aluminium material
2. Making patterns or models of impeller products from wax materials. The pattern or model follows the size, shape and details of the final product impeller
3. Dipping or dyeing wax patterns in ceramic slurry liquid until the formation of ceramic molding

4. De-waxing or melting wax with a boiler from inside the ceramic molding, leaving empty space or cavity or cavity impeller shape like wax pattern
5. Ceramic sintering molding to dry it and harden the ceramic cavity mold
6. Pouring molten metal into a hard ceramic cavity and waiting for the metal to solidify
7. Release of impeller product casting objects from ceramic molding
8. Finishing and machining impeller products into impeller products according to design.

The impeller investment casting process follows the flowchart shown in Figure 1.

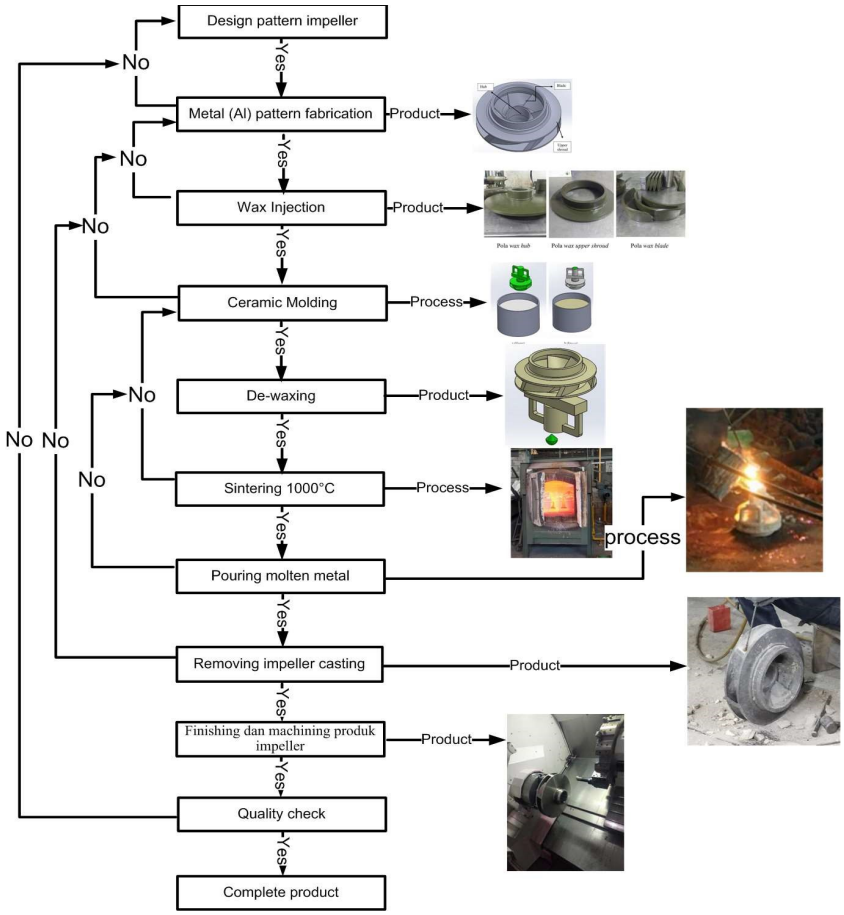

Figure 1. Investment casting fabrication process of pump impeller

3. Results and Discussion

3. 1 Paternt fabrication or Impeller closed pattern

The closed impeller is a design type used in BB3 3-stage centrifugal pumps. The closed impeller features blades that fully cover its backside. This means that the fluid entering the impeller cannot flow back towards the source or the pump's suction side.

The blades close completely, the fluid is forced to move in the outward direction with a slight leak into the suction side. This results in a higher pressure at the pump output, which is useful in overcoming greater system pressures or pumping fluid to higher altitudes. The geometric impeller is shown in Figure 2.

In the impeller casting process, as shown in Figure 2, the impeller's geometry is created as a pattern and divided into three parts to form a wax replica of the impeller. These parts include the hub (as depicted in Figure 3), the upper shroud (as shown in Figure 4), and the wax mold for the impeller blades (illustrated in Figure 5).

The metal patterns, as shown in Figures 3, 4, and 5, are created with larger dimensions, considering the material shrinkage percentage, wax shrinkage percentage, and machining allowances. Therefore, the size of these metal patterns consists of the impeller size + material shrinkage percentage of the impeller + wax shrinkage percentage + the additional dimensions for further machining processes. Dimensions of the impeller are adjusted by adding material shrinkage following ASTM A-743 CF3M (SS316L) standard, wax shrinkage, and machining allowances. Shrinkage values: SS316L material = 2.5~3.5%, wax = 1%, and machining allowance = 5 mm.

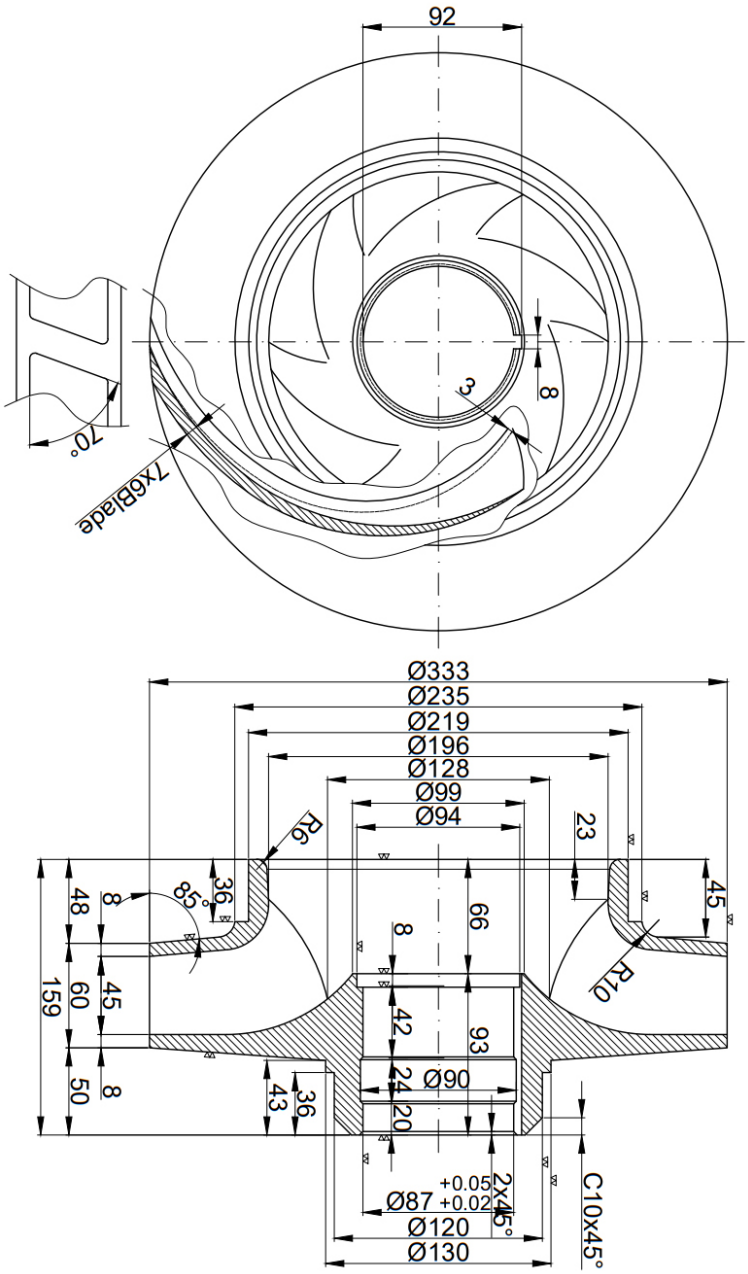

Figure 2. Impeller closed geometric

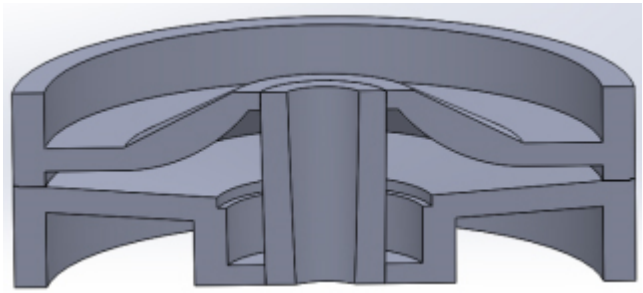

Figure 3. Hub impeller dies

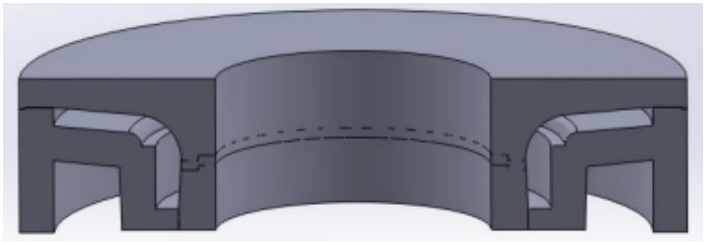

Figure 4. Upper shroud of impeller

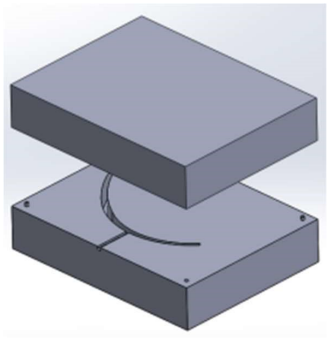

Figure 5. Blade impeller dies

3. 2 Impeller replica fabrication

The wax pattern replicas are created by injecting PARAMELT CERITA 996C AS wax into designated aluminium dies, as shown in Figures 3, 4, and 5. The molten wax, at a temperature of 80°C, is injected into the aluminium impeller mold through an injection nozzle at a temperature of 60 - 70°C from the injection machine, at an injection pressure of 10 – 70 kg/cm2. The wax replicas resulting from the injection process are removed from the metal impeller mold. The dimensions of the wax replica impeller are measured to ensure that they match the intended dimensions of the impeller to be produced. The outcomes of the injection for forming the impeller parts are illustrated in Figure 6.

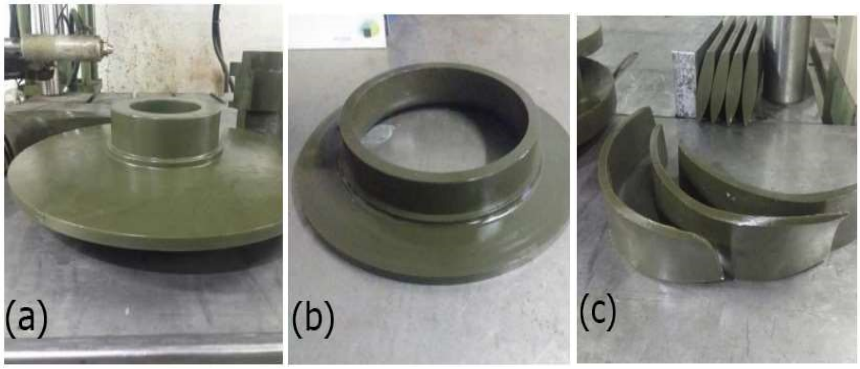

Figure 6. Wax pattern of impeller, (a) Hub, (b) Upper shroud, (c) Blade

3. 3 Sistem gating fabrication

The gating system, or runner system, serves the purpose of directing molten metal into the mold cavity. Figure 7 illustrates the geometric design of the gating system for molding the impeller, which consists of three parts: the pouring cup, runner, and gas vent.

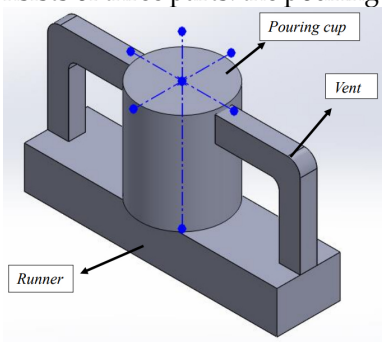

Figure 7. Gating system of impeller moulding

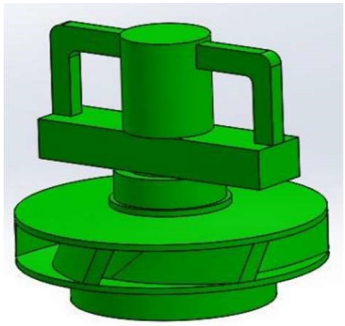

Figure 8. Form of wax pattern assembling

3. 4 Wax pattern assembly

Assembling is the process of joining or combining the pattern parts fabricated from wax to form a single unit. Assembly is performed by heating solder on the elements, then simultaneously melting the solder on the surface of the runner and the main gating (the largest module) of the workpiece and bonding them together. The assembly configuration of the wax pattern to form the molding impeller is illustrated in Figure 8.

Table 1. Ceramic forming dyeing material

Materials	Stages of Immersion						
	1	2	3	4	5	6	7
Colloidal silica, Liter	18	18	24	24	24	24	24
Wetting agent, cc	20						
Anti Foam, cc	40						
Zircon foam, kg	80						
Zircon flour, kg		80					
Sand/stucco	yes	yes	yes	yes	yes	yes	yes
Mullite sand, #200, kg			60	60	60	60	60
Viscosity, second	20-45	25-35	25-40	25-40	25-40	25-40	25-40
Drying temperature, °C	23-27	23-27	23-27	23-27	23-27	23-27	23-27
Drying time,hours	24	2 - 4	2 - 3	2- 3	2 -3	2 - 3	2 -3

3. 5 Investment casting mold ceramic fabrication

The assembled wax pattern is dipped into a slurry and stucco mixture. In this process, it is dipped seven times to obtain a ceramic layer adhering to the wax pattern, with a thickness of 9 – 10.5 mm. Afterward, it is left to dry to form the cavity mold.

Slury materials for dyeing are shown in Table 1.

3. 6 De-waxing

The wax pattern is melted and removed from the ceramic mold, leaving behind the cavity mold of the complete impeller with the gate system. The de-waxing process is carried out in an autoclave boiler. Steam is used to melt the wax, at a pressure of 8-10 kg/cm2, for a duration of 10 minutes. The de-waxing process results in the formation of channels and empty spaces, forming the impeller's shape, as well as the gating system.

3. 7 Sintering ceramic mold

Sintering is the process of firing the ceramic mold in an oven at temperatures around 1000°C for approximately 4 hours, gradually. The goal is to obtain a hard and strong mold and to remove any remaining water and wax residues from the de-waxing process. During the sintering process, particles of ceramic material within the mold begin to interact chemically and physically. This results in the bonding and crystallization of particles, which helps enhance the strength and hardness of the ceramic mold.

3. 8 Molten metal pouring

The cavity of the impeller mold is now ready to be filled with molten metal. The raw material or metal to be used in this case, ASTM A-743 CF3M (SS316L), is melted using an induction furnace. The melting process reaches a temperature equal to or greater than 1500°C.

3. 9 Removing impeller casting

The removal of the casting impeller from the mold cavity is done by destroying the ceramic mold. This is followed by cleaning, trimming excess metal, and cutting off the gating system.

3. 10 Quality inspection of casting objects

The inspection is carried out visually to ensure that there are no defects or cracks of the impeller casting object. Dimensional and geometric examination of impeller casting objects, guided by impeller design drawings.

3. 11 Machining

Machining is carried out to achieve precise measurements according to the casting design drawings. The main parts of the impeller e.g. the hub that will pair with other components, for example the shaft must meet tolerances according to the impeller pair.

4. Conclusion

The fabrication and design of the pump impeller were conducted using the investment casting method. The investment casting process encompasses various stages, which include crafting a metal pattern from aluminum. The creation of the aluminum metal pattern is achieved through machining with additional dimensions. The dimensions of the metal pattern are determined by adding the dimensional sizes, accounting for the material shrinkage of SS316L (2.5~3.5%), wax shrinkage (1%), and machining (5mm). Wax patterns are individually crafted for distinct parts of the impeller, and then assembled into a complete wax pattern that aligns with the impeller's geometry, inclusive of the gating system.

Dipping in Slurry and Stucco: The wax pattern undergoes repetitive immersion in a slurry and stucco mixture until a thick ceramic layer envelops the wax impeller pattern.

Wax Pattern Melting: The wax pattern is melted out from the ceramic mold, leaving behind cavities that replicate the impeller's geometry.

Sintering of Ceramic Mold: The ceramic mold of the impeller is subjected to sintering at 1000°C to form a robust ceramic mold with cavities primed to receive molten metal.

Metal Pouring, Solidification, and Removal: Molten metal is poured into the cavities, allowed to solidify, and subsequently extracted from the ceramic mold.

The resulting cast impeller is now prepared for the machining process.

Acknowledgements

The author expresses his gratitude to PT. Trieka Aimex who has given the opportunity, provided the place and facilities to carry out this design and research work.

Funding: "This research received no external funding". This study received no specific funding from government, commercial, or non-profit organizations.

Conflicts of Interest: "The authors declare no conflict of interest."

References

1. Critchley, D. Investment casting. in *Manufacturing Engineer* vol. 71 26–27 (1992).
2. Chen, Y. *et al.* Researches on the pyrolyzing strength of gelcasting Al2O3-based ceramic molds for double-wall blade. *J. Am. Ceram. Soc.* **102**, 7564–7574 (2019).
3. Miao, K., Lu, Z., Jing, H., Li, D. & Yin, M. Creep Control of U-Bends Cores of Integral Ceramic Molds During Presintering. *J. Am. Ceram. Soc.* **97**, 3380–3383 (2014).
4. Venkat, Y., Choudary, K. R., Das, D. K., Pandey, A. K. & Singh, S. Ceramic shell moulds for investment casting of low-pressure turbine rotor blisk. *Ceram. Int.* **47**, 5663–5670 (2021).
5. Venkat, Y., Hazari, N., Baig, M. A. H., Singh, S. & Das, N. Mullite shell mould for casting of advanced CG and SX components in nickel based superalloys. *Int. J. Cast Met. Res.* **26**, 114–121 (2013).
6. Barbosa, J. & Puga, H. Ultrasonic melt processing in the low pressure investment casting of Al alloys. *J. Mater. Process. Technol.* **244**, 150–156 (2017).
7. Lopes, V. *et al.* Magnesium stents manufacturing: Experimental application of a novel hybrid thin-walled investment casting approach. *J. Mater. Process. Technol.* **299**, 117339 (2022).
8. Gromada, M., ̄wieca, A., Kostecki, M., Olszyna, A. & Cygan, R. Ceramic cores for turbine blades via injection moulding. *J. Mater. Process. Technol.* **220**, 107–112 (2015).
9. Dong, Y. W., Li, X. L., Zhao, Q., Yang, J. & Dao, M. Modeling of shrinkage during investment casting of thin-walled hollow turbine blades. *J. Mater. Process. Technol.* **244**, 190–203 (2017).
10. Szeliga, D. *et al.* Investigation of casting–ceramic shell mold interface thermal resistance during solidification process of nickel based superalloy. *Exp. Therm. Fluid Sci.* **87**, 149–160 (2017).
11. Xiang, R., Li, Y., Li, S., Xue, Z. & Yuan, L. New insight into treatment of foundry waste: porous insulating refractory based on waste foundry sand via a sacrificial fugitive route. *J. Aust. Ceram. Soc.* **57**, 427–433 (2021).
12. Chen, Z., Xu, G., Cui, H., Zhang, X. & Zhan, X. Preparation of porous Al2O3 ceramics by starch consolidation casting method. *Int. J. Appl. Ceram. Technol.* **15**, 1550–1558 (2018).

RiESTech
Recent in Engineering Science and Technology

MBI

Article

Analysis of The Testing Sequence for A 3,000 Watt Electric Motorcycle Using The Taguchi Method

Genia Auberta [1], Muslimin [1*], M. Prasha Risfi Silitonga [1], Daniel Janthinus Kristianto [2], Wan Mansor Bin Wan Muhamad [3], Muhammad Aziz [4]

[1] 1 Program Studi Manufaktur, Jurusan Teknik Mesin, Politeknik Negeri Jakarta, Jl. Prof. G. A. Siwabessy, Kampus UI, Depok 16425, Indonesia
[2] PT. XYZ Kawasan B II E, Jl. Raya Inti Blok C3 No. 12, Cibatu, Cikarang Selatan, Bekasi Regency, West Java 17550, Indonesia
[3] Universiti Kuala Lumpur Kampus Cawangan Malaysia France Institute, Malaysia
[4] Institute of Industrial Science, The University of Tokyo, Japan
* Correspondence: muslimin@mesin.pnj.ac.id

Abstract: Electric vehicle manufacturers have a significant need for brushless DC (BLDC) motors. This is because of its benefits, including brushless construction, high efficiency and power ratio, huge mass, and ease of control. This study aims to examine the relative importance of the various var-iables on the three motorcycles that the three prototypes are actually mounted on. In order to op-timize the technical testing process and save wasteful time and expense, the Taguchi Method with the characteristic of smaller is better was employed for the research. Two different types of road terrain were used for the tests: flat and uphill with slope angles of 2 and 4. Use. Prototypes 1, 2, and 3 of the electric motors utilized in this study each feature a distinct ratio of magnetic poles: prototype 1 has 48 poles/54 slots, prototypes 2 has 50 poles/45 slots, and prototype 3 has 40 poles/36 slots. According to the test results, the type of electric motor, the type of road, the dis-tance, and ultimately the speed level are the parameters that have the greatest influence.

Keywords: BLDC Electrric Motor 1; Taguchi Method 2; Magnet Pole 3; Types of Road 4; Travel Distance 5; Level Speed 6;

Citation:. Genia Auberta, Muslimin, M. Prasha Risfi Silitonga, Daniel Janthinus Kristianto, Wan Mansor Bin Wan Muhamad, & Muhammad Aziz. (2023). Analysis of The Testing Sequence for A 3,000 Watt Electric Motorcycle Using The Taguchi Method. Recent in Engineering Science and Technology, 1(04), 20–25. https://doi.org/10.59511/riestech.v1i04.35

Academic Editor: Iwan Susanto

Received: 26 September 2023
Accepted: 16 Oktober 2023
Published: 30 Oktober 2023

Publisher's Note: MBI stays neutral with regard to jurisdictional claims in published maps and institutional affiliations.

1. Introduction

Indonesia has proposed to achieve carbon neutrality by 2060, supported by a 45% reduction in carbon dioxide (CO2) emissions by 2030 compared to 2010 levels and an expansion of renewable energy in the electricity, transportation, and industrial sectors [1]. President of Indonesia, Joko Widodo, plans to make Indonesia one of the global centers for electric vehicle manufacturing [2]. As of November 2022, the Ministry of Energy and Mineral Resources (ESDM) recorded approximately 25,782 electric motorcycles in Indonesia, both for personal and conventional use [3].

The government's efforts to support the achievement of carbon neutrality are outlined in the Regulation of the Minister of Energy and Mineral Resources of the Republic of Indonesia No. 3 of 2023, which states that the government will provide support through conversion workshops covering at least battery costs, Brushless Direct Current (BLDC) motors, and controllers that match the battery power capacity and engine wattage details [4]. There is a significant demand for Brushless Direct Current (BLDC) motors in the electric vehicle industry [5], supported by their advantages in performance, high power-to-weight ratio, ease of handling, and longer lifespan.

In the automotive industry, PT XYZ, a company operating in this sector, needs to enhance its products to accommodate these changes. A study was conducted to support these changes, such as analyzing the electric vehicle market at the Indonesia Electric Motor Show (IEMS) 2022. Observations made during the event revealed that out of 43 electric two-wheeler brands operating in Indonesia, none were using local BLDC motors. This situation encouraged PT XYZ to innovate and establish local production and development of BLDC motors, particularly BLDC motors with a maximum continuous power of 3000W.

PT XYZ designed three prototypes with different magnet poles numbers: prototype 1 with 48 poles/54 slots, prototype 2 with 50 poles/45 slots, and prototype 3 with 40 poles/36 slots. The pole combinations were selected based on the simplest three-phase coil topology to implement [6]. Different pole combinations have the effect of reducing voltage, current, and power values while improving efficiency [7]. These three BLDC prototypes were applied to electric motorcycles, resulting in different power requirements, with power consumption being influenced by road conditions and driving speed [8].

Hence, dynamic testing is needed to assess the performance of electric motorcycles and determine the power consumed on flat roads and steep inclines [9]. This research aims to determine the sequence of factors that most affect dynamic testing, specifically on flat roads and two steep roads with inclinations of 2° and 4° based on The American Association of State Highway and Transportation Officials (AASHTO) standards for urban roads [10]. The distance variations used in this study are 60 meters, 120 meters, and 180 meters, with road inclinations not exceeding 200 meters [11]. This study aims to identify the order of factors that have the most influence on the testing of three prototype electric motors installed on electric motorcycles to determine which product is the most optimal.

2. Materials and Experiment Methods

The flowchart for this research begins with a literature review, followed by the determination of testing using the Taguchi Method, which will result in a summarized testing scheme. Next, there is the preparation of the Brushless Direct Current (BLDC) motor on the electric motorcycle, followed by an initial check of the motorcycle's functionality. Subsequently, tools and materials for testing are prepared, and the BLDC motor is tested on three different road terrains. The data obtained from testing is then analyzed using statistical analysis based on the Taguchi Method, which determines the sequence of the most influential factors in the research. Finally, the research concludes with the selection of the most optimal prototype using statistical analysis based on the Taguchi Signal-to-Noise (S/N) Ratio.

Determination of Testing Using the Taguchi Method

The completion stages to produce a testing scheme in this research consist of the following:

a. In the initial stage of this research, the determination of the testing output is conducted, where the desired output in this study is the average power consumption result for each prototype.
b. Next is the selection of the testing factors to be conducted. In this stage, an analysis of the factors influencing the optimal testing process for two-wheeled electric vehicles is performed. Several factors are used in this research, as shown in Table 1.

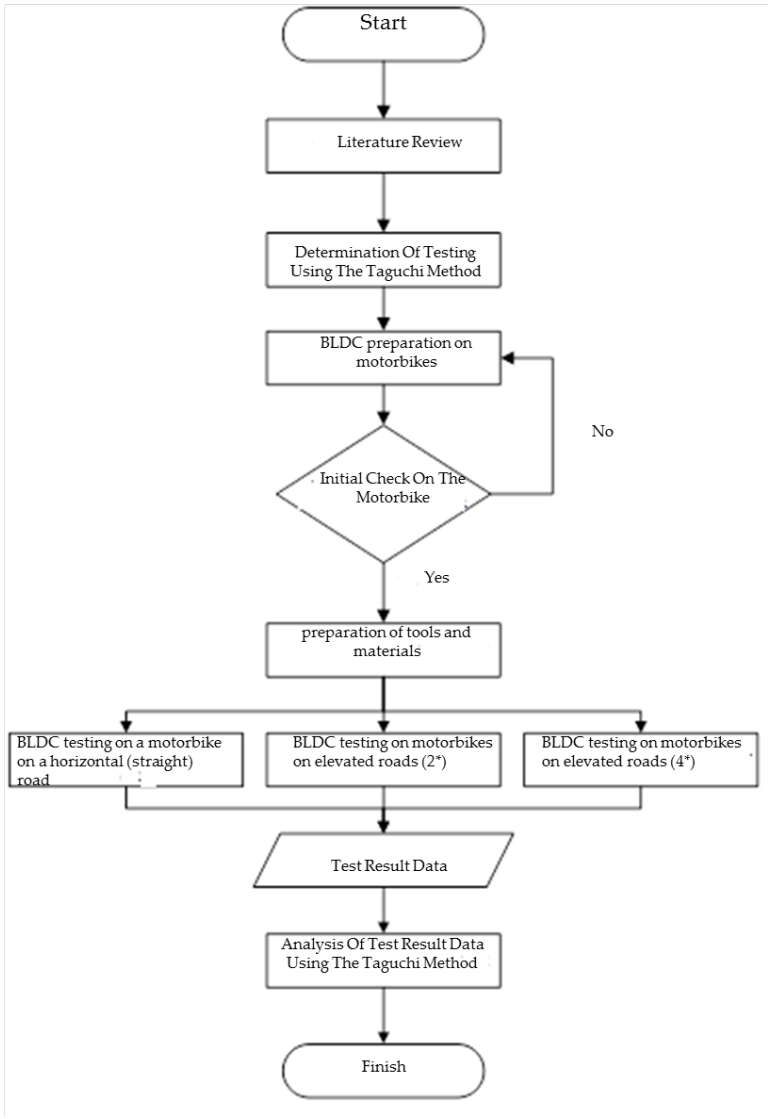

Figure 1. Research Flowchart

Table 1. Testing Factors

Control Factors	Variation		
	Level 1	Level 2	Level 3
Types of Electric Motors (A)	40 Poles Magnet	48 Poles Magnet	50 Poles Magnet
Road Terrain (B)	Flat	Elevation 2°	Elevation 4°
Distance (C)	60 m	120 m	180 m
Speed (D)	Speed 1	Speed 2	Speed 3

c. The determination of uncontrollable factors (noise factors) and their variations is then carried out.

d. The selection of an orthogonal array, which helps reduce the number of experiments conducted. For example, in this study, there are 4 controlled variables with 3 variations, which means that using a conservative method would require running 3^4 = 81 simulations. However, with the Taguchi method, the number of tests is reduced to only 9. This reduction is based on the calculation of the degrees of freedom of the observed factors, as follows: Degrees of Freedom = (Number of Levels) - 1 (1)

In this case, the degrees of freedom for each factor and the total degrees of freedom for the study result in a total value of 8. The selection of the appropriate matrix for the experiment is determined by the calculation of the degrees of freedom, and the L_9 orthogonal matrix (3^4) is suitable and sufficient for use in this research [12].

e. The final step is to create a testing scheme using the orthogonal array table [13].

Test Results Data

The real-time testing results of the electric motorcycle with the assistance of testing equipment will display the magnitude of the input power, where power is expressed as [9]. The test sequence is shown in Table 2.

$$P = I \times V \quad (2)$$

Where:
P = power (Watt)
I = current strength (A)
V = voltage (V)

Table 2. Electric Motor Testing Scheme for BLDC

Process Flow	Illustration
Start	
Motorcycle Checck	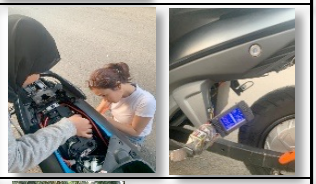
Installation of Personal Protective Equipment	
Start the Motorcycle	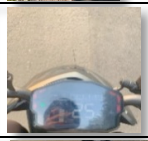
Run the Motorcycle	
Return the Motorcycle to the Starting Distance	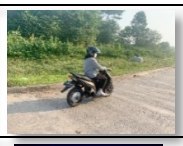
Check Power Meter	
End	

Analysis of Test Results Data Using the Taguchi Method

The testing results that have been conducted will be analyzed using the Taguchi Method to determine the influencing factors and the optimal factor levels. The analysis takes into account the impact of the factors, and the author develops equations based on the book "A Primer on the Taguchi Method" [13].

3. Results and Discussion

Testing Using the Taguchi Method

After conducting the testing according to the orthogonal array matrix, the average power output values obtained from all experiments are shown in Table 3.

Table 3. Testing Factors

Experiment No.	Column				Power Output (Watt)
	Jenis Motor (A)	Medan Jalan (B)	Jarak (C)	Speed	
1	40 Poles Magnet	Flat	60 m	Speed 1	473,89
2	40 Poles Magnet	Elevation 2˚	120 m	Speed 2	690,73
3	40 Poles Magnet	Elevation 4˚	180 m	Speed 3	1031,09
4	48 Poles Magnet	Flat	120 m	Speed 3	347,18
5	48 Poles Magnet	Elevation 2˚	180 m	Speed 1	334,38
6	48 Poles Magnet	Elevation 4˚	60 m	Speed 2	322,24
7	50 Poles Magnet	Flat	180 m	Speed 2	238,00
8	50 Poles Magnet	Elevation 2˚	60 m	Speed 3	262,06
9	50 Poles Magnet	Elevation 4˚	120 m	Speed 1	469,35

Analysis of Test Results Data Using the Taguchi Method

Calculation of the influence of factor levels on the output power of the electric motor. The calculation results are shown in Table 4, which reveals the optimum factors with the characteristic response of the average output power of the electric motor, where "smaller is better" then the calculation will subsequently be plotted on the curve depicted in Figure 2 using Minitab Statistical Software.

Table 4. Testing Factors

Level	A	B	C	D
1	731,90	353,02	352,73	425,87
2	334,60	429,06	502,42	416,99
3	323,14	607,56	534,49	546,78
Difference	408,77	254,53	181,76	129,79
Ranking	**1**	**2**	**3**	**4**

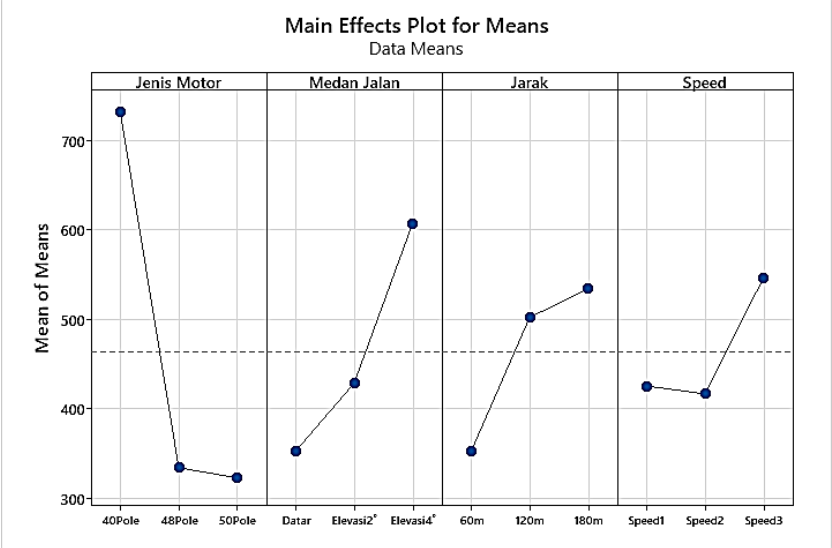

Figure 2. Main Effects Plot for Means

The results of the Taguchi Method analysis conclude that the order of factors influencing the average output power of the electric motor with the "smaller is better" characteristic is factor A (motor type), B (road terrain), C (distance), and D (speed).

4. Conclusions

The application of the Taguchi Method to direct testing on flat and uphill road terrains with elevation angles of 2° and 4° yields the order of the most influential factors, namely the type of electric motor used, road terrain, distance, and speed level. Direct testing with the assistance of the Taguchi Method reveals that the largest average output power, with a value of 1031.09 Watts, occurs with the 40-poles motor type, a 4° uphill terrain, a distance of 180 meters, and a speed level of 3.

Acknowledgments: The author expresses gratitude to PT XYZ for their support and assistance in conducting the research and/or writing of this article.

References

1. C. Transparency, "Laporan Climate Transparency : Membandingkan Aksi Iklim G20 Menuju Net Zero," 2021. Accessed: Mar. 19, 2023. [Online]. Available: https://www.climate-transparency.org/wp-content/uploads/2021/11/Indonesia-Country-Profile-2021_Bahasa.pdf
2. M. Fauzia, "Cita-cita Jokowi : Jadikan Indonesia Pusat Industri Mobil Listrik Dunia," Kompas.com, Nov. 28, 2019. https://money.kompas.com/read/2019/11/28/201656626/cita-cita-jokowi-jadikan-indonesia-pusat-industri-mobil-listrik-dunia (accessed Feb. 08, 2023).
3. I. Giovani, "Penasaran Sudah Berapa Jumlah Kendaraan Listrik di RI? Ini Datanya," IDN Times, Dec. 07, 2022. https://www.idntimes.com/automotive/car/ilh-1665114296-ogx/penasaran-sudah-berapa-jumlah-kendaraan-listrik-di-ri-ini-datanya (accessed Feb. 08, 2023).
4. H. EBTKE, "Telah Terbit: Permen ESDM Nomor 3 Tahun 2023 Tentang Pedoman Umum Bantuan Pemerintah dalam Program Konversi Sepeda Motor dengan Penggerak Motor Bakar menjadi Sepeda Motor Listrik Berbasis Baterai," EBTKE H, Mar. 30, 2023. https://ebtke.esdm.go.id/post/2023/03/31/3457/telah.terbit.permen.esdm.nomor.3.tahun.2023.tentang.pedoman.umum.bantuan.pemerintah.dalam.program.konversi.sepeda.motor.dengan.penggerak.motor.bakar.menjadi.sepeda.motor.listrik.berbasis.baterai (accessed Jul. 04, 2023).
5. A. Cahyadi, D. Pembimbing Dimas Anton Asfani, D. Candra Riawan, and D. TEKNIK ELEKTRO Fakultas Teknologi Elektro, "OPTIMALISASI DESAIN MOTOR BRUSHLESS DC 1 KW UNTUK MENGURANGI TORSI COGGING PADA KENDARAAN LISTRIK," 2019.
6. J. Soulard, F. Libert, and J. Soulard, "Investigation on Pole-Slot Combinations for Permanent-Magnet Machines with Concentrated Windings," 2004. [Online]. Available: https://www.researchgate.net/publication/237458473
7. M. Irfan, R. F. Ariyanto, L. Syafaah, A. Faruq, Nurhadi, and N. Subeki, "Stator slotted design of axial flux permanent magnet generator for low-speed turbine," in IOP Conference Series: Materials Science and Engineering, Institute of Physics Publishing, May 2020. doi: 10.1088/1757-899X/821/1/012027.
8. E. Prasetyo, D. Dahlan, D. Raditya, and N. Fadhli, "Analisis Pengujian Sepeda Motor Listrik 3 kW Pada Jalan Mendatar dan Menanjak," Seminar Rekayasa Teknologi SEMRESTEK , 2018.
9. R. N. Fadhli, "ANALISIS KONSUMSI ENERGI PADA SEPEDA MOTOR LISTRIK 3 kW," 2018.
10. T. A. Polus, T. J. Craus, and T. M.Livneh, "DETERMINATION OF LONGITUDINAL GRADES ON RURAL ROADS," Israel Institute of Technology, 1998.
11. K. PUPR, "LINGKAR NAGREG H-10 DIFUNGSIKAN," 2010.
12. Nanda. Laysvania, "ANALISA OPTIMASI PROSES HEAT TREATMENT PRODUK FASTENER DENGAN METODE TAGUCHI DAN NEURAL NETWORK," 2017.
13. R. K. Roy, A primer on the Taguchi method. Society of Manufacturing Engineers, 2010.

RiESTech
Recent in Engineering Science and Technology

MBI

Article

Analysis in 3D Rendering Modeling Processing using Autodesk Maya and Blender Software

Suhaili Muhammad [1,*], Khairusani Nabila Fitri [1]

[1] Creative Media State Polytechnic, Indonesia
* Correspondence: suhaili@polimedia.ac.id

Abstract: Many alternative software for producing 3D animation. Some of them are Autodesk Maya and Blender. In the animation pipeline there are three main stages, namely pre-production, production and post-production. In post-production there are rendering or rendering steps. Rendering is the processing of all animated scene objects in the form of modeling data, movement, texturing, lighting, sound and so on into a certain output which is the final appearance of an animated video. In this research, we analyze the performance of the two 3D software above in rendering an object. Rendering using Autodesk Maya takes 45 seconds. While the results of rendering using Blender can complete in 1 second. In terms of rendering quality, Autodesk Maya produces more detailed texturing quality.

Keywords: 3D Rendering; Autodesk; Maya; Blender Software

Citation:. Muhammad, S., & Nabila Fitri, K. (2023). Analysis in 3D Rendering Modeling Processing using Autodesk Maya and Blender Software. Recent in Engineering Science and Technology, 1(04), 26 – 30. https://doi.org/10.59511/riestech.v1i04.30

Academic Editor: Iwan Susanto

Received: 26 September 2023
Accepted: 16 Oktober 2023
Published: 31 Oktober 2023

Publisher's Note: MBI stays neutral with regard to jurisdictional claims in published maps and institutional affiliations.

1. Introduction

Animation is a collection of images arranged in an orderly manner so as to create a movement with a predetermined calculation. Animation has various types one of which is 3D animation. In this era, 3D animation has developed quite rapidly. This development is marked by the large number of 3D animation works circulating among the public, in the form of films, television series, video games, and even advertisements. 3D animation itself has the meaning of creating moving images from a collection of 3-dimensional images that can be seen from several perspectives and points of view. Making 3D animation can use various software, one of the software for making 3D animation is Autodesk Maya and Blender. In making 3D animation the same as with other types of animation that still uses 12 principles of animation, pre-production, production and post-production. In post-production there are Render or rendering stages. Rendering is the processing of all animated scene objects in the form of modeling data, movement, texturing, lighting, sound and so on into a certain output which is the final appearance of an animated video. In this process, 3D animation is illustrated into a realistic display by simulating real-world principles. Determine the direction of the light that will be reflected or hit, the texture of an object, the blur effect, the color and so on to simulate like in the real world or be changed with a card style and so on.

2. Materials and Experiment Methods

In this study the authors used a qualitative method by analyzing the 3D rendering process in Autodesk Maya and Blender software. The research data was obtained from observing books, journals, articles as well as social media platforms that discussed rendering processing in the two softwares.

2.1. Rendering process on Autodesk Maya software

In the process of rendering the Audosek Maya software, there are many textures in the software. Some of these textures such as blinn, lambert, Arnold and others. In general, using Arnold's texture rendering to simulate textures more like those in the real world or use a cartoon style. The steps or how to render on Maya Arnold are as follows:

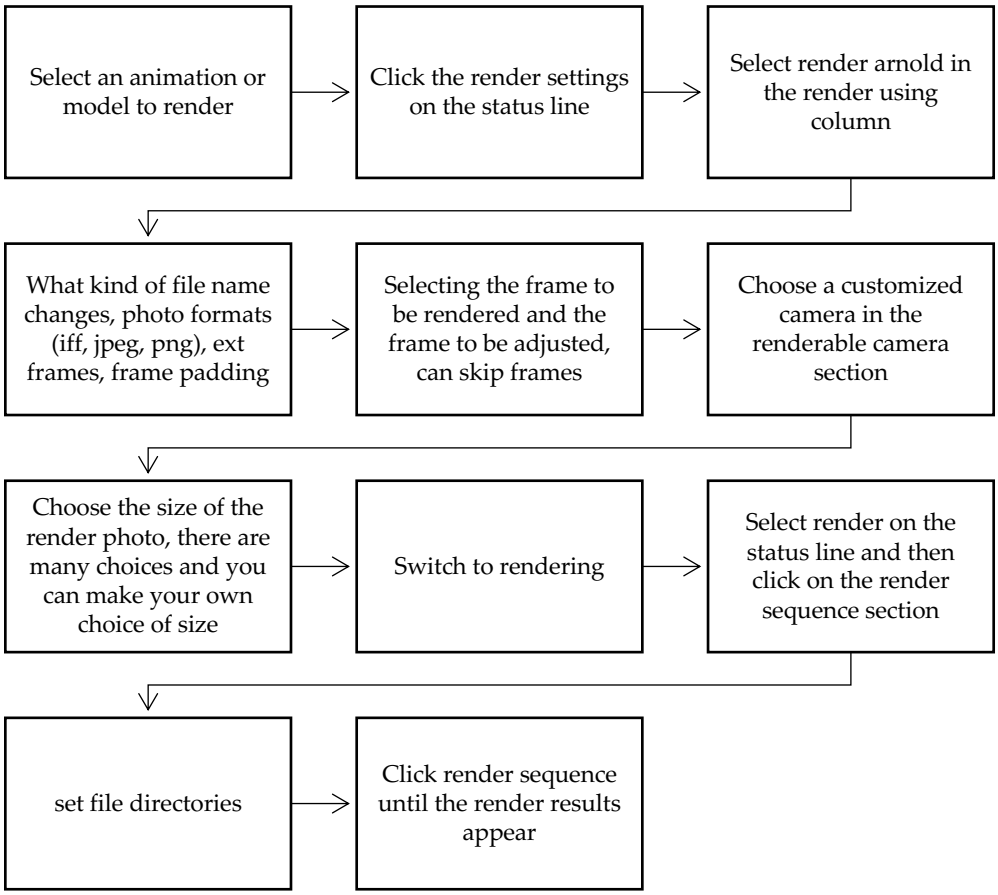

Figure 1. Step or how to render on Maya Arnold

2.2. Rendering process in Blender software

As with the rendering process of the Audosek Maya software, there are also many textures in the blender software. These textures are like eevee, workbench and cycles. Blender's rendering process is almost similar to Arnold's, who adjusts the settings first. At the blender rendering stage using rendering eevee. The steps or how to render in the Eevee Blender are as follows :

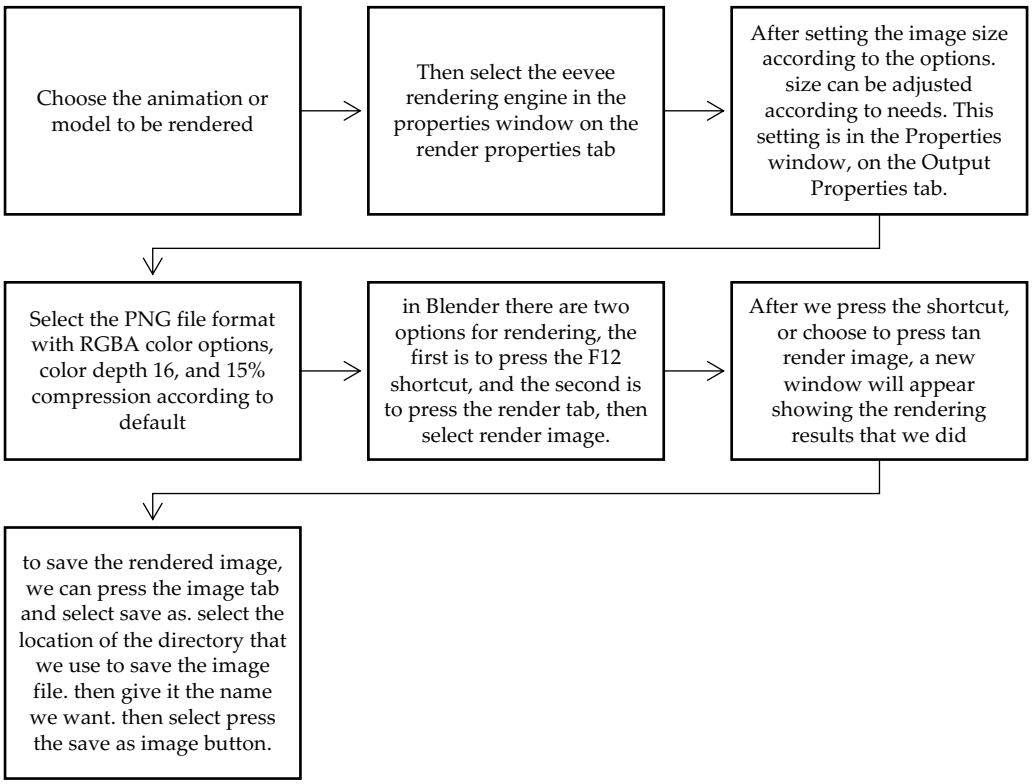

Figure 2. Step or how to render on Eevee Blender

3. Results and Discussion

From the second stage of the Autodesk Maya and Blender software above, the rendering process produces several differences. The following is the result of rendering processing from both software.

Table 1. rendering results of Autodesk Maya and Blender

Software	Result	Processing Time
Autodesk Maya (render Arnold)		45 seconds
Blender (render Eevee)		1 seconds

In terms of speed, time duration and quality of visual results. Autodesk Maya takes 45 seconds to render an image object. Meanwhile, the duration of image rendering processing in Blender is only 1 second. In terms of quality, rendering using Autodesk Maya displays detailed image texture results. Whereas in Blender the quality of the image rendering results looks soft and the texture is not detailed.

Rendering on Autodesk Maya using the Arnold texture function besides taking quite a long time is also quite heavy. Especially if you use CPU-based hardware only. Therefore it is recommended that when rendering Maya Arnold, you can upgrade it by adding a GPU device. As for rendering in blender using the texture function eevee has quite light characteristics. However, in terms of the completeness of the features or tools in Blender, it is still more complex than the Autodesk Maya software.

4. Conclusions

From the rendering process between Autodesk Maya and Blender software, both have their own characteristics. For the needs of an animation project, you can do a combination of the two software to produce a satisfactory rendering with good performance. For example, when carrying out the process of making modeling, rigging and animation, you can use Autodesk Maya software. Furthermore, when doing the rendering process, you can use the Blender software. But back again to the needs of each creator for the theme of a project.

Supplementary Materials: The following supporting information can be downloaded at: www.mbi.com/xxx/xx, Figure S1: title; Table S1: title; Video S1: title.

Author Contributions: For research articles with several authors, a short paragraph specifying their individual contributions must be provided. The following statements should be used "Conceptualization, A.A.; methodology, A.A.; software, B.B.; validation, A.A., B.B. and C.C.; formal analysis, C.C.; investigation, D.D.; resources, C.C.; data curation, A.A.; writing—original draft preparation, B.B.; writing—review and editing, A.A.; visualization, B.B.; supervision, C.C.; project administration, X.X.; funding acquisition, Y.Y. All authors have read and agreed to the published version of the manuscript." Authorship must be limited to those who have contributed substantially to the work reported.

Funding: Please add: "This research received no external funding" or "This research was funded by NAME OF FUNDER, grant number XXX" and "The APC was funded by XXX".
It is not necessary to include specifics about the program or the types of grants and awards. When funding comes from a block grant or other resources available to a university, college, or other research institution, include the name of the institute or organization that provided the funding.
If no funding has been provided for the research, include the following sentence: This study received no specific funding from government, commercial, or non-profit organizations.

Acknowledgments: In this section, you can acknowledge any support given which is not covered by the author contribution or funding sections. This may include administrative and technical support, or donations in kind (e.g., materials used for experiments).

Conflicts of Interest: Declare any conflicts of interest or state, "The authors declare no conflict of interest." Authors must identify and declare any personal circumstances or conflicts of interest that could be interpreted as inappropriately influencing the representation or interpretation of reported research results. Any role played by the funders in the design of the study, data collection, analysis, or interpretation, manuscript writing, or decision to publish the results must be declared in this section. If there is no role, please state, "The funders had no role in the design of the study; data collection, analysis, or interpretation; manuscript writing; or decision to publish the results."

Appendix A

The appendix is an optional section that can contain details and data that are not included in the main text, such as explanations of experimental details that would disrupt the flow of the main text but are still necessary for understanding and reproducing the research shown; figures of replicates for experiments with representative data shown in the main text can be added here if brief, or as Supplementary data. Appendices can contain mathematical proofs of results that are not central to the paper.

References

1. Ids international school. "Apa itu animasi". Last modified September 7, 2022. https://idseducation.com/apa-itu-animasi/
2. Ids international school. "memahami lebih dalam pengertian animasi 3d". Last modified August 26, 2022. https://idseducation.com/memahami-lebih-dalam-pengertian-animasi-3d/
3. Aria, Perdana. "Apa pengertian render dalam mendesain model 3D" 2019 on Qoura. https://id.quora.com/Apa-pengertian-render-dalam-mendesain-model-3D
4. Setyo, Prihatmoko. "15 Perangkat Lunak Rendering 3D terbaik untuk Para Pemula". Published May 11, 2022. http://desain-grafis-s1.stekom.ac.id/informasi/baca/15-perangkat-lunak-rendering-3D-terbaik-untuk-para-profesional/3ffe509517936b27abdb5cb74f219bbbf5c7e221
5. Autodesk Maya . "How to improve render times with Arnold and Maya" published November 12, 2020. https://knowledge.autodesk.com/support/maya/troubleshooting/caas/sfdcarticles/sfdcarticles/How-to-improve-render-times-with-Arnold-and-Maya.html
6. IRender GPU. "Improve render time with arnold for maya" Last modified June 9, 2022.https://irendering.net/improve-render-time-with-arnold-for-maya/
7. Dipta, Mahardika. "Tutorial Rendering Gambar Pada Blender 3.0" published January 14, 2022. https://www.gamelab.id/news/1365-tutorial-rendering-gambar-pada-blender-30

RiESTech
Recent in Engineering Science and Technology

MBI

Article

Analysis of Solar Photovoltaic System Related to Daily Energy and PV Sizing at Mekartani Farm

Cherly Zahara Siregar [1], Tatun Hayatun Nufus [1], Cecep Slamet Abadi [1], Sonki Prasetya [1*]

[1] Program Studi Sarjana Terapan Teknologi Rekayasa Konversi Energi, Jurusan Teknik Mesin, Politeknik Negeri Jakarta, Jl. Prof. G. A. Siwabessy, Kampus UI, Depok 16425, Indonesia
* Correspondence: sonki.prasetya@mesin.pnj.ac.id

Abstract: Mekartani Farm is a comunity located at Jl. Mataram III RW06, Kelurahan Mekar Jaya, Kecamatan Sukmajaya, Depok City, West Java Mekartani Farm is managed by Mr. Ferryzar. The implementation of PLTS aims to reduce the electricity costs that are still charged to local residents due to planting activities. The study analyzed solar irradiation data as well as data on total electricity loads and daily energy needs at the Mekartani Farm. The PLTS system designed at the Mekartani Farm is capable of generating 1347.7 kWh of energy in a year and has batteries with a capacity of 100 Ah, three of which are arranged in parallel to provide a backup for two days of autonomy. Using a 400 WP solar panel of two parallel-set units with an efficiency of 20.57%.

Keywords: Mekartani Farm; Hydroponics; PLTS; Components PLTS

1. Introduction

Hydroponic farming system is an efficient method of agriculture, where plants grow without utilizing soil. Currently, hydroponic cultivation has become an alternative for urban communities. This is because this method is considered highly effective for those who want to meet their daily needs for fresh, healthy, and natural vegetables [1].

Electricity is a primary resource in everyday human life. The human demand for electricity continues to increase over time, posing future challenges. Electricity usage in hydroponics is essential for supplying water pumps for hydroponic plant irrigation, typically obtained from the national electricity grid. The main energy source for electricity generation partly comes from fossil fuels such as coal or natural gas, which are known to be non-renewable and environmentally unfriendly. Additionally, according to Government Regulation No. 15 of 2022, the coal mining industry is one of the sectors subject to taxes (PLTS) [2].

Solar energy can be converted into electrical power through Solar Photovoltaic Systems (PV systems) [3]. This system harnesses sunlight as an energy source to generate electricity. To perform this conversion, components like solar cells (Photovoltaic or PV) are required [4]. In this way, the electrical power generated by solar panels can be utilized in hydroponic farming practices. Therefore, the approach used is to combine electrical power from the national grid with the energy generated by solar panels, aiming for sustainable electrical energy conservation for the future [5].

Mekartani Farm is an area managed by a community under the leadership of Mr. Ferryzar. It is located amidst residential areas on Mataram III Street, specifically at the Secretariat Office of RT. 05 RW. 016, Mekar Jaya Village, Sukmajaya Subdistrict, Depok City, West Java. Mekartani Farm has a daily load of 2619.8 Wh. With the issue of electricity

Citation: Prasetya , S., Abadi, C. S., Siregar, C. Z., & Nufus, T. H. (2023). Analysis of Solar Photovoltaic System Related to Daily Energy and PV Sizing at Mekartani Farm. Recent in Engineering Science and Technology, 1(04), 31–37. Retrieved from https://www.mbi-journals.com/index.php/riestech/article/view/34

Academic Editor: Iwan Susanto

Received: 26 September 2023
Accepted: 16 Oktober 2023
Published: 31 Oktober 2023

Publisher's Note: MBI stays neutral with regard to jurisdictional claims in published maps and institutional affiliations.

costs still borne by the surrounding residents and to reduce greenhouse gas emissions in support of the government's goal of achieving Net Zero Emissions by 2060, the planning of a Solar Photovoltaic System (PLTS) at Mekartani Farm is the objective [6].

2. Materials and Experiment Methods

1.1 Flow Chart

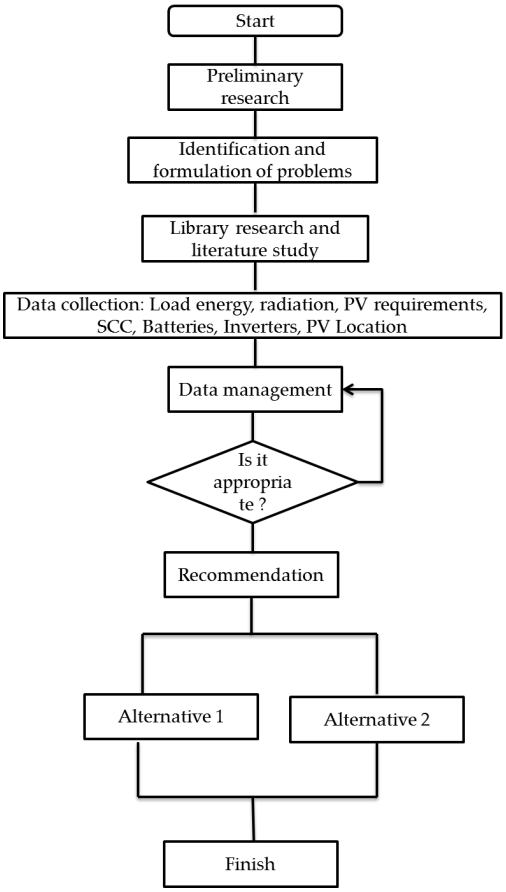

Figure 1. Illustrates the stages undertaken in this research.

It begins with the planning process, followed by establishing the background for the research, identifying the problem, and formulating the problem to provide a clear direction for the study. The next step involves conducting a literature review related to the proposed design, as well as collecting data, including daily load data and solar irradiance data. Once the data is obtained, the author can process it and provide recommendations based on the research findings.

1.2 Photovoltaic Module

The fundamental component in solar power generation is the solar cell, which serves to convert solar radiation into an electrical current. This cell consists of a thin layer of semiconductor material, typically made of silicon, with a thickness of about 0.3 mm and a size ranging from 100 to 225 cm^2. Silicon possesses tetravalent properties, meaning it has 4 valence electrons [7]. The silicon layer is doped with valence atoms (referred to as P-type) on one side and other valence atoms (referred to as N-type) on the other side. This results in an excess of holes in the P-type region and an excess of electrons in the N-type region. The presence of holes and electrons creates an electron flow when sunlight touches the solar cell [5].

1.3 Determining the Capacity of PV System Components

1.3.1 Determining Power Requirements

By calculating the power required by each equipment to be supplied by the PV System and the number of hours of usage per day, this calculation yields power in watts per day. The load calculation can be done using the following equation:

Total Load = (Load Equipment × Daily Hours of Use (W)) × Inverter Efficiency (Joules per Ampere)

1.3.2 Batteries

1. Calculating Battery Energy Requirements

The calculated energy is the amount to be drawn from the battery. Data needed includes the autonomy period, which is determined based on the local weather conditions. In areas frequently covered by clouds, such as mountainous regions, it's recommended to use a three-day autonomy period. In areas with mostly clear weather throughout the year, a two-day autonomy period is sufficient. There is a formula used to calculate the battery energy requirements with the equation [8]:

Battery Energy Requirements = Total Daily Energy Requirements (Wh) × (Autonomy Days)

2. Determining Working Voltage and Calculating Battery Ampere-Hour (AH)

For the load power capacity, it can be determined by considering whether it's daytime or nighttime and the load quantity (Watt).

3. Determining Working Voltage and Calculating Battery Ampere-Hour (AH)

The data required pertains to battery and inverter specifications, as well as the calculated battery energy requirements. It's necessary to determine the voltage (Vdc), Ampere-Hour (AH), and Battery Depth of Discharge (DOD). The formula used is:In the process of designing a grated coconut drying chamber, several tools are used to complete the design process. After the design process is completed, airflow simulation is conducted within the drying chamber. The following are the tools used in the process of designing the drying chamber and simulating the airflow.

$$Number\ of\ battery\ series\ = \frac{System\ Working\ Voltage\ (Vdc)}{Battery\ unit\ Working\ Voltage(Vdc)}$$

$$Parallel\ Number\ of\ batteries = \frac{Energy\ requirements\ from\ the\ battery\ (Wh)}{System\ voltage(Vdc)x\ Battery\ AH\ xx\ DOD}$$

Battery Depth of Discharge (DOD): The maximum depth to which a battery can be discharged without causing damage, typically expressed as a percentage of its total capacity.

Solar Panels

The initial step in determining the required components is to obtain daily load data and solar irradiance at the solar panel installation location. Processing the data from the operating load, the energy load can be calculated using the following equation [8]:

Total Energy = Daytime Energy + Nighttime Energy

Once the total energy for the module is obtained, we must then determine the lowest daily average irradiance. After obtaining data on the lowest daily irradiance, we can determine the required PV capacity using the following equation [9]:

$$Ptotal = \frac{Module\ Enegy}{Gavg} \times Gstc$$

Where:

Gavg = Average daily solar irradiance
Gstc = Solar irradiance under Standard Test Conditions (1 kW/m^2)
The effective area mentioned here is the specific area for placing solar modules, excluding areas for installation ease, maintenance, as well as space for power houses, distance from fences, and so on. The data needed includes the solar module efficiency, and the effective area can be calculated using the formula [8]:

$$area(m2) = \frac{kwp}{(Solar\ Module\ Efficiency)}$$

kWp = Peak power of the solar module

To determine the maximum number of PVs to be installed, you can use the following formula:

$$\text{Number of Modules} = \frac{Total\ Wp}{Wp/\ module}$$

Total Wp = Peak power of the solar module
Wp/Module = Power used in the solar module
Choosing the Appropriate Inverter for the Required Power

1.3.4 The consideration
Selecting an inverter that matches the required power is done using the formula:

$$\text{Watt (VA)} = \text{Wmax} + (25\% \times \text{Wmax})$$

Where:

Wmax: Maximum power (Watt)
25%: Reserves for the starting power of electrical devices.

1.3.5 Calculating Power Capacity and SCC Current

Input power and SCC (Solar Charge Controller) current are determined by the peak power of the solar module (Wp), while output power and SCC current are determined by the battery system's operating voltage (Vdc) [10].
The total SCC power must be greater than the total daily energy:

$$Total\ SCC\ current\ >\ from\ calculation = \frac{Total\ energy\ (W)}{Battery\ system\ Working\ Voltage\ (Vdc)}$$

$$\text{The number of SCC units needed} = \frac{\text{Total SCC Current}}{\text{SCC Current Capacity}}$$

SCC power can be calculated as follows:

$$\text{SCC Power} = \frac{\text{Total Energy (W))}}{\text{Number of Units}} \text{ Watts/SCC}$$

3. Results and Discussion

3.1 Measurement of Equipment and Loads at Mekartani Farm

Table 1. Daily Load Data for Mekartani Farm

No.	Type Of Equipment/Load	Amount	Load Power (Watt)	Total Load Power	Daily Operations (Hour) Afternoon	Daily Operations (Hour) Night	Daily Energy Requirements Per Load (Wh) Afternoon	Daily Energy Requirements Per Load (Wh) Night	Total Daily Energy Requirements (Wh)	
1	Water Pump	2	27.6	55.2	10	14	552	772.8	1324.8	
2	Sperinkle Pump	1	22	22	0.3	0.2	6.6	4.4	11	
3	Lamp	4	10.8	43.2		13		561.6	561.6	
4	arduino	1	10	10	10	14	100	140	240	
5	cctv	1	5.1	5.1	10	14	51	71.4	122.4	
6	modem	1	15	15	10	14	150	210	360	
				90.5			**859.6**	**1760.2**	**2619.8**	Wh
									2.6198	kWh
							Effisiensi 25%		**3274.75**	Wh
	Total								**3.27475**	kWh

From Table 1, it is explained that the daily energy requirement during the daytime is 859.6 Wh, and during the nighttime, it is 1760.2 Wh. Therefore, the total daily energy requirement at Mekartani Farm is 2619.8 Wh or 2.62 kWh. After adding a 25% efficiency factor, the daily energy requirement at Mekartani Farm becomes 3.27 kWh.

3.2 Graph Between Daily Load and Solar Irradiance at Mekartani Farm

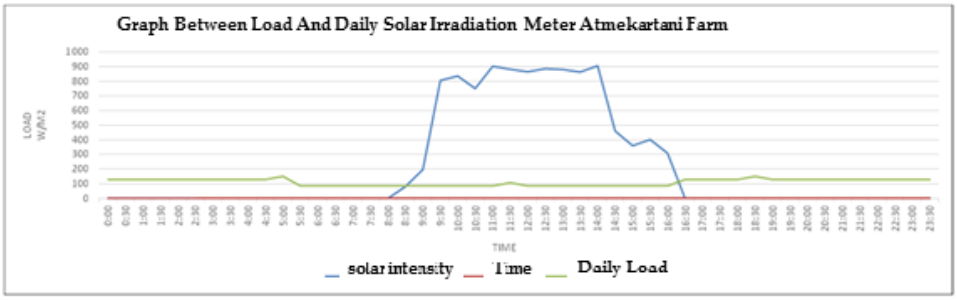

Figure 2. Graph of Daily Load and Solar Irradiance at Mekartani Farm

Figure 2: Explains that daily solar irradiance data is collected from 08:30 AM to 04:00 PM, with data taken every 30 minutes. The highest solar irradiance occurs at 2:00 PM (W/m2). Meanwhile, from the graph, it can be observed that the daily load increases at 05:00 AM and 06:00 PM by 150.5 Wh due to the use of sprinklers for hydroponic plant irrigation during those hours. The average daily solar irradiance at Mekartani Farm is 5.19 kWh/m2.

3.3 Calculation of Solar Photovoltaic System (PLTS) Requirements

a. Calculating Peak Power

$$Kwh\ (peak) = \frac{Total\ Daily\ Energy\ (kWh)}{Daily\ average\ irradiation}$$

$$= \frac{2{,}6198}{5{,}1893} = 0.505\ \text{kWp}$$

The value needs to be multiplied by system losses of 15% - 25%.
The peak power value after accounting for system losses becomes 0.631 kWp.kW (peak) PLTS = 0.631 kWp = 631 Wp

b. Choosing a Solar Module

$$Area\ (m^2) = \frac{0.631\ kWp}{21\%}$$

The solar module area = effective area x 2 = 3 square meters x 2 = 6 square meters

c. Calculating the Number of Modules

$$Number\ of\ Modules = \frac{Peak\ Power\ of\ Solar\ Modules\ (Total\ Wp)}{(Wp/Module)}$$

$$Number\ of\ Modules = \frac{(631\ Wp)}{(400\ Wp)} = 1.6\ or\ 2\ solar\ modules$$

d. Calculating Battery Energy Requirements and Battery Capacity

Battery energy requirements = 2620 Wh x 2 days
Battery energy requirements = 5240 Wh

$$Parallel\ Number\ of\ batteries = \frac{5239.6\ (Wh)}{24Vdc\ x\ 100\ Ah\ x\ 80\%)} = 2{,}729 \sim 3$$

e. Calculating Power Capacity and Current of the Solar Charge Controller (SCC)

The Charge Controller capacity with a total energy of 765.9 Watts, and the system operating voltage is 24Vdc, and a SCC with a current capacity of 30 Amperes is chosen
The total SCC power must be above 631.05 Watts

$$Total\ SCC\ current\ >\ from\ calculation = \frac{631.05\ W}{24\ Vdc} = 26.29\ A$$

$$Number\ of\ SCC\ units\ required = \frac{26.29\ A}{30} = 0.87\ units, rounded\ to\ 1\ Unit$$

$$SCC\ power\ can\ be\ calculated = (631.05\ W)/(1\ unit) = 631.05\ Watt/SCC$$

f. Choosing the Inverter

The capacity of the PLTS inverter at Mekartani Farm is as follows:
Capacity Inverter = 90.5 Watts + (25% x 90.5 Watts) = 113.125 Watts
Therefore, the required inverter capacity should be greater than 113.125 Watts. The selected inverter capacity is 1,000 watts.

4. Conclusions

Based on the results of the calculation analysis of the PLTS design system at Mekartani Farm, the components chosen for daily energy needs of 2.6 kWh are solar modules with a capacity of 400 Wp with a total of 2 units, a 1 kW inverter for 1 unit, a 24vdc battery with a capacity of 100Ah. 3 units and and 1 unit SCC 30 A.

Acknowledgments: The author would like to express his gratitude to Mr. Ferryzar and the team for their assistance and support in collecting data and providing locations for carrying out this scientific activity. Thank you also to Mrs. Tatun, Mr. Haolia Rahman Ph.D as the supervisor for the research and writing of this scientific work.

References

1. S. Prasetya, H. M. Ridlwan, M. Muslimin, and R. Khairunnisa, "PENGEMBANGAN BUDIDAYA TANAMAN ORGANIK DENGAN SISTEM HIDROPONIK OTOMATIS BAGI MASYARAKAT PERKOTAAN (Kelurahan Munjul)," Mitra Akademia: Jurnal Pengabdian Masyarakat, vol. 3, no. 1, 06/15 2020, doi: 10.32722/mapnj.v3i1.2829.
2. N. Hidayah, "Inilah Tarif PPh 22 Batubara dan Cara Menghitung, Lengkap!," 1 Februari. [Online]. Available: https://mekari.com/blog/pph-22-batubara/#:~:text=Tarif%20Pajak%20Penghasilan%20atau%20PPh,dan%20tidak%20termasuk%20nilai%20PPN
3. D. J. E. B. T. D. K. Energi and K. S. D. Mineral, Panduan Pengelolaan Lingkungan Pembangkit Listrik Tenaga Surya (PLTS), 2020.
4. S. P. Adji Chandra Prasetyo, Yuli Mafendro Dedet Eka Saputra, "Analisis Safety Factor pada Frame Mobile SPBKLU Berbasis PLTS sebagai Sumber SPBKLU," 2022. [Online]. Available: https://scholar.google.co.id/citations?view_op=view_citation&hl=id&user=h6OtK_cAAAAJ&cstart=20&pagesize=80&citft=1&email_for_op=cherlysiregar25%40gmail.com&citation_for_view=h6OtK_cAAAAJ:g5m5HwL7SMYC.
5. J. Hasyim Asy'ari1, Angga3. "INTENSITAS CAHAYA MATAHARI TERHADAP DAYA KELUARAN PANEL SEL SURYA." https://publikasiilmiah.ums.ac.id/bitstream/handle/11617/3930/E08.pdf?sequence=1&isAllowed=y (accessed.
6. K. K. R. Indonesia, "Ini Komitmen Indonesia Mencapai Net Zero Emission," 24 November 2022. [Online]. Available: https://www.kemenkeu.go.id/informasi-publik/publikasi/berita-utama/Ini-Komitmen-Indonesia-Mencapai-Net-Zero-Emission
7. Y. T. Rendra Yonatan Nikijuluw#1, Murtiyanto Santoso#3, "Perencanaan Sizing dan Analisa Biaya Energi Sistem PLTS di Komunitas Desa Muara Langon, Kabupaten Paser, Kalimantan Timur," Journal Teknik Elektro, vol. Volume 9 No. 2, p. 6, 2 September 2016. [Online]. Available: https://media.neliti.com/media/publications/140662-ID-perencanaan-sizing-dan-analisa-biaya-ene.pdf.
8. B. Kencana et al., PANDUAN STUDI KELAYAKAN PEMBANGKIT LISTRIK TENAGA SURYA (PLTS)TERPUSAT, 2018.
9. B. P. b. Rak Skunpong a, "A Practical Method for Quickly PV Sizing," Science Direct, vol. 8, 31 March 2011. [Online]. Available: https://www.sciencedirect.com/science/article/pii/S1877705811000361#section-cited-by.
10. S. P. Auffanida Fadhila Permana, Yuli Mafendro Dedet Eka Saputra, "Studi Pendahuluan Sistem PLTS Off Grid Sebagai Sumber Mobile SPBKLU," 2022. [Online]. Available: https://scholar.google.co.id/citations?view_op=view_citation&hl=id&user=h6OtK_cAAAAJ&sortby=pubdate&citation_for_view=h6OtK_cAAAAJ:70eg2SAEIzsC.

PT. Mencerdaskan Bangsa Indonesia

PT MENCERDASKAN BANGSA INDONESIA (MBI), 4th Floor Gedung STC Senayan Room 31-34, Jl. Asia Afrika Pintu IX, Jakarta 10270, Indonesia.